FACULTY OF SCIENCE
UNIVERSITY OF COPENHAGEN

Multi-Messenger Probes of the Sources of Ultra-High Energy Cosmic Rays

Taus Munk Hansen

Master's Thesis in Physics

Supervisor: Assi. Prof. Markus Ahlers

Co-supervisor: Postdoc. Mohamad Rameez

Niels Bohr Institute

University of Copenhagen

Date: April 23, 2019

Abstract

In spite of decades of research, the origin of ultra-high energy cosmic rays (UHECRs) still remains uncertain. It has long been hypothesized that UHECR sources might also leave a footprint in the form of high-energy gamma-rays and neutrinos. IceCube, the world's first km^3-sized neutrino telescope, recently reported the observation of an astrophysical flux of neutrinos, paving the way for using high-energy astrophysical neutrinos as an aide in the quest of uncovering the sources of UHECRs. In this thesis, we implement two different methods of correlating the arrival directions of neutrinos and UHECRs, and compare the sensitivity of these joint methods to the sensitivity of neutrino (ν)-only and cosmic ray (CR)-only methods. We find that the joint methods by themselves are less effective than the combined sensitivity of the ν- and CR-only methods. By modifying the joint methods through the removal of neutrinos assumed to be uncorrelated with UHECRs, we find that one of the joint methods provides improved sensitivity over the combined sensitivities of the ν- and CR-only methods. Finally, we also evaluate lower bounds on the density of UHECR sources using public data from the Pierre Auger Observatory and the Telescope Array Project, obtaining our best bound of $\rho_{lower} = 1.44 \cdot 10^{-4}\mathrm{Mpc}^{-3}$ for a characteristic UHECR deflection angle of $\theta = 3^{\circ}$.

ACKNOWLEDGEMENTS

I extend my sincerest gratitude to my supervisors Markus Ahlers and Mohamed Rameez for their guidance and patience during the countless hours they spent helping me understand both the theory and results of this project. It is no exaggeration to say that the completion of this project would have been impossible without them.

I am also eternally grateful to those who took the time to read and offer me feedback on my thesis, including my supervisors, Abdurrahman Barzinji, Charlotte Rosenstrøm and Lea Halser.

I also extend my gratitude to my family for being supportive and understanding, especially during the writing process. This also entails friends and family who allowed me to rant after long days.

A warm thanks is also extended to my dorm neighbors, with whom I've spent many a late night unwinding after a long day at the university.

Finally, I would like to thank my fellow Master's students from my office, namely Greg Gold, David Damgaard, Henrik Munch and Johannes Mønsted Sørensen, including Abdurrahman, Charlotte and Lea, for creating the lovely environment within which I worked on my thesis.

CONTENTS

1 INTRODUCTION

One of the greater mysteries in astronomy pertains to the origin of ultra-high energy cosmic rays (UHECRs), ionized particles with energies at $\sim 10^{20}$eV or above, comparable to that of a baseball thrown by a professional. In spite of the fact that cosmic rays (CRs) were discovered more than a century ago [1], and that the first UHECR with $E > 10^{20}$eV was discovered over half a century ago [2], the pinpointing of UHECR sources has as of yet proven unsuccessful. This is in large part due to CRs being deflected by Galactic and extragalactic magnetic fields during propagation, leading to arbitrarily large angular displacement from the point of origin for all but the most energetic UHECRs. These energetic UHECRs, with energies in excess of $E = 5 \cdot 10^{19}$ eV, have increased interaction cross-sections with the cosmic microwave background (CMB), which rapidly attenuates them out of this energy regime. This effect is called the Greisen-Zatsepin-Kuz'min (GZK) effect [3, 4], and it sets an effective limit of the distance propagated by any UHECR with $E > 5 \cdot 10^{19}$, which in turn also sets an effective limit on the magnetic deflection they experience.

Unfortunately, UHECRs with such high energies are extremely sparse, and only a few hundred have been observed in total, distributed across the celestial sphere with no statistically significant anisotropies [5]. Compounding the difficulties of working with such a small data sample is the large uncertainties related to the magnetic field strengths and coherence lengths of the Galactic and extragalactic magnetic fields [6, 7]. In addition, there are also uncertainties on the composition of UHECRs [8], i.e. whether they are lighter nuclei such as protons, or heavier nuclei such as iron. Thankfully, it is expected that the UHECRs should also leave clues of the location of their point of origin in the form of secondary particles stemming from UHECRs interacting with ambient gas and radiation fields in the source region [9]. These secondaries take the form of high-energy neutrinos and gamma rays, both of which should point directly back to their origin. Unfortunately, gamma rays have very short interaction lengths in intergalactic space, which leaves the neutrinos as the primary candidate for assisting in the search of UHECR sources. This is doubly true because high-energy neutrinos necessitate the presence of high-energy CRs, while gamma rays can stem from both hadronic and leptonic processes [10].

The current leader in neutrino astronomy is the IceCube Neutrino Telescope [11], which was the first neutrino observatory to ever discover the presence of a high-energy astrophysical neutrino flux [12]. This astrophysical flux is consistent with certain calorimetric models of CR acceleration. In addition, IceCube also indirectly discovered the first confirmed source of high-energy CRs with its detection of a neutrino event from the blazar TXS 0506+056 in 2017 [13]. With these recent discoveries, neutrino astronomy has unquestionably proven its capacity to meaningfully contribute to our understanding of extragalactic astrophysics, and it is only a matter of time before even more powerful next-generation neutrino telescopes will improve the possibilities in neutrino astronomy [14, 15].

With all this in mind, an attempt to correlate the arrival directions of high-energy neutrinos and UHECRs seems obvious, and this has in fact already been attempted. Using the observational data from the two primary UHECR observatories along with astrophysical neutrino data of IceCube, a correlational analysis has been carried out in 2015, showing no statistically significant correlation [10]. The sample size of both UHECRs and neutrinos is constantly increasing, however, and it should only be a matter of time before detection of neutrino point sources becomes commonplace.

The purpose of this thesis is to investigate different methods of analysis used to locate the point sources of UHECRs in an attempt to improve upon current methodology. This will be accomplished through the implementation of Monte Carlo simulations that realistically recreate a series of source distribution and observational scenarios, using the density of the sources and the number of observed particles as the primary variables of the analysis. The resulting data will be utilized in analyses using neutrinos and UHECRs seperately, as well as in a joint analysis wherein the neutrinos and UHECRs will be correlated with each other using two different methods. In addition to benchmarking these different methods, two tasks will be undertaken. Firstly, density bounds will be set on the population of UHECR sources using public data from the two premier UHECR observatories [5]. Secondly, we will investigate the strength of a method to 'clean' a neutrino data sample from neutrinos uncorrelated with UHECRs before correlating the two.

The outline of this thesis is as follows: First, a brief introduction is given to the concept of multimessenger astronomy in Section 2. In Section 3, we elaborate on the multimessenger connection between UHECRs and high-energy neutrinos, justifying the correlation of the two. In Section 4 we present and derive the mathematical theory behind the implementation and statistical analysis. In Section 5, we describe how the implementation was made, and outline the primary assumptions and simplifications made during implementation. In Section 6, we describe the method specific to the neutrino-only analysis and present the results of the analysis. In Section 7, we describe the method specific to the CR-only analysis and present the results of the simulation-only analysis, and then the results of the analysis using real UHECR data. In Section 8, we describe the methods specific to the joint analyses, and present the results in comparison to the other methods. The section also includes the results of the 'cleaning' method. Finally, we discuss the outlook based on our results and conclude the thesis in Section 9.

2 FUNDAMENTALS OF MULTI-MESSENGER ASTRONOMY

Until recently, detections, observations and analyses of astrophysical phenomena have been carried out through the study of extraterrestrial electromagnetic emission. While these astrophysical phenomena emit a variety of different messengers other than just photons, namely cosmic rays (CRs), neutrinos and gravitational waves (GWs), it has proved exceedingly difficult to conclusively link observations of these messengers to known source candidates. Notable exceptions include CRs associated with solar flares, neutrino bursts associated with the supernova (SN) SN1987a [16, 17, 18] and a 290TeV neutrino event from the blazar TXS 0506+056 [13]. However, with the recent emergence of neutrino detectors [19, 11, 20] and the first GW detector [21], along with the construction of modern CR observatories [22, 23], we are entering a new era in astronomy: the multi-messenger era. In this section, a short introduction will be given to the three new messengers in astronomy, focused on CRs and neutrinos. GWs will be given a very brief introduction, and an introduction to the already well-established photons will be omitted.

2.1 *Cosmic rays*

In the early 1910's, it was discovered that the Earth is under constant bombardment by charged particle radiation of extraterrestrial origin [1]. This radiation, dubbed cosmic rays (CRs) consists of highly energetic, electrically charged particles, such as ionized nuclei and electrons. As they enter the Earth's atmosphere, they can interact with other particles, and initiate a cascade of secondary, tertiary etc. particles. These particles can be detected by large shower arrays on the ground, and from them, the energy and the arrival direction of the progenitor CR can be inferred. It should be noted that for low energy CRs, it is possible to directly measure the primaries. This holds true for energies up to about 1 PeV. While CRs have been known to exist for more than a century and have been subject to vast scientific inquiry, very few sources of CRs are known. This is because the arrival direction of the progenitor CR does not necessarily correspond to the direction of the CR source. This is due to the electrically charged nature of CRs, which causes them to be deflected by galactic and (where applicable) extragalactic magnetic fields, making it all but impossible to reliably evaluate the point of origin for the average CR [8]. Fortunately, the most energetic protons with $E > 5 \cdot 10^{19}$ eV experience enhancement in the inelastic interaction cross section with the cosmic microwave background (CMB) due to the Δ-resonance, which sets an effective limit on their propagation length, and thus also the degree to which they are magnetically deflected. Thanks to this property, such CRs are currently being studied extensively. CRs subject to this phenomenon, called the Greisen-Zatsepin-Kuz'min (GZK) effect [3, 4], are a subset of what is called Ultra-High Energy Cosmic Rays (UHECRs, CRs with $E > 10^{18}$ eV). UHECR's will be the primary CR focus in this thesis, and will be discussed in detail in Section 3.0.2.

2.1.1 *Astrophysical sources*

CRs have a wide range of possible sources, ranging from solar CRs produced during solar flares (though technically these are called 'Solar Energetic Particles'), Galactic CRs produced in for instance supernova explosions, supernova remnants (SNRs) and Wolf-Rayet stars, and finally to extragalactic CRs that can be produced in a wide range of possible sources such as the intergalactic medium (IGM), gamma-ray bursts (GRBs), active galactic nuclei (AGNs) and blazars [8, 24]. In spite of this varied cast of candidates, the Sun remains the only confirmed source of an observed CR flux, and only indirect evidence of other CR sources exists [13, 25]. The aforementioned UHECRs are thought to stem from extragalactic sources, specifically GRBs and AGNs of those mentioned, while less energetic CRs could be of both Galactic as well as extragalactic origin [8, 24].

2.1.2 *Means of observation*

CR detectors vary greatly depending on the energy-range they are designed to investigate. Low-energy CRs can be detected for instance through space telescopes like the AMS[26]. We will focus on higher-energy CRs, like UHECRs, which are primarily detected through air shower arrays with surface arrays of particle detectors, for instance using water Cherenkov detectors. These detect the cascade particles from an air shower associated with a CR. UHECRs are primarily detected by the two most sensitive UHECR detectors today, namely the Pierre Auger Observatory (PAO) located in the Mendoza Province, Argentina, and the Telescope Array (TA) located in Utah, USA. Both detectors are hybrid detectors, having both a surface array of particle detectors as well as flourescence telescopes. Flourescence telescopes measure luminescence from air showers, and these measurements can also be used to infer the properties of the progenitor CR [27].

PAO is the largest air shower detector ever built with 1600 water-Cherenkov detectors in a triangular-grid pattern spaced over 3000 km^2. In addition, PAO has four stations each with six flourescence telescopes. The PAO has specifically been designed to detect CRs exceeding 10^{19} eV, and as such provides the best data available on UHECRs of any detector in the world [22].

TA has a surface array consisting of 507 scintillation detectors covering 700km^2 surrounded by 3 flourescence detectors. While smaller than PAO, it still provides data on UHECRS in addition to data on CRs at lower energies, extending down to 10^{16} eV [23].

2.2 *Neutrinos*

Neutrinos are fermions that do not interact through the strong nuclear force, making them leptons. Neutrinos, unlike their electron, muon and tau counterparts, have no electrical charge. Thus neutrinos do not interact through the electromagnetic force either. This leaves neutrinos with the two weakest forces through which they interact: the gravitational force, and the weak nuclear force [27]. For this reason, neutrinos are largely unaffected as they propagate through the universe and unlike CRs, neutrinos point directly back to their point of origin. This is true even when the origin is electromagnetically unobservable, for instance if it were wrapped in dense molecular clouds. While this is a very desirable trait, the downside is that neutrinos are exceedingly difficult to detect - a common qualitative statement being that the mean free path of a neutrino with an energy of $E = 1$GeV propagating through lead is $\lambda = \frac{1}{\sigma n} \approx 1\,\mathrm{AU}$, where σ is the neutrino cross section, n is the number density of lead, and 1AU is an astronomical unit, equal to the average distance from the earth to the sun. While this is a vast oversimplification, as neutrino-nucleon cross sections increase with neutrino energy, it underlines the main point: detection of neutrinos is a massive challenge.

Neutrinos in the Standard Model exist in 3 flavors, the electron neutrinos ν_e, the muon neutrino ν_μ and the tau neutrino ν_τ, and all three neutrinos have a corresponding antiparticle. Until recently, neutrinos were assumed to be massless, but observations from the Super-Kamiokande neutrino observatory have shown evidence of neutrino oscillation - meaning the oscillation between neutrino flavour states [18]. The existence of such oscillations requires a nonzero rest mass, however both the absolute mass scale and the mechanism that generates their mass are unknown. More open questions remain on the topic of neutrinos, such as whether they are Dirac or Majorana particles [27].

2.2.1 *Astrophysical sources*

Thus far, only three sources of astrophysical neutrinos have been confirmed, namely the Sun, SN1987a and TXS 0506+056. With that being said, a multitude of neutrino sources have been hypothesized. As this thesis is primarily interested in high energy neutrinos, the possible sources for low-energy neutrinos, such as solar neutrinos, will not be discussed. Potential high energy neutrino sources include supernova remnants (SNRs), dense molecular clouds, gamma-ray binaries, pulsar wind nebulae, microquasars, active galactic nuclei (AGNs) and gamma ray bursts (GRBs) among others [9]. These sources are, where applicable, thought to be both Galactic and extragalactic, with SNRs thought to be the dominant contributor to the Galactic high energy neutrino flux, and AGNs along with GRBs being the dominant contributors to the extragalactic flux. Finally, neutrinos stemming from the decay products of ultra-high energy cosmic rays in transit, called *cosmogenic neutrinos*, are also thought to exist, and should have extremely high energies [9]. The mechanisms behind cosmogenic neutrinos will be described in Section 3.0.2.

2.2.2 *Means of observation*

Neutrino detectors are primarily Cherenkov detectors with large volumes to maximize the probability of neutrino interaction within the detector. Currently active large-scale detectors include the IceCube Neutrino Observatory on the South Pole[11], ANTARES in France[20] and Super-Kamiokande (SuperK) in Japan [19]. Like with CR detectors, neutrino detectors are optimized for specific tasks, with ANTARES and SuperK both specialized in detecting subsets of neutrinos in energy ranges that are less likely to correlate with UHECRs.

IceCube is the primary candidate for observation of neutrinos that could correlate with UHECRs, as the telescope itself is optimized for detection of neutrinos at energies above 100TeV and is sensitive to energies up to EeV [11]. The telescope is a km^3-sized Cherenkov detector embedded in ice at a depth of $1450 - 2450\,\mathrm{m}$

below the surface. Photon detection is achieved by the use of 5160 photomultiplier tubes (PMTs), divided evenly between 86 cables (called 'strings') spaced with a characteristic length of 125 m apart, resulting in km^2 of coverage. The detector began collecting data using a partially finished configuration in April 2005, with more strings being added gradually to the data collection until its completion in December 2010.

2.3 *Gravitational waves*

Gravitational waves are essentially propagating disturbances in the curvature of space-time caused by accelerating matter. This 'radiation' propagates unhindered, save for the same characteristics seen in EM waves, namely with intensity scaling as $1/r^2$. GWs are notoriously difficult to detect, as the measurable quantity related to them, the strain (the relative degree to which matter is 'elongated'), is of the order 10^{-21}, and it was not before the 14th of September, 2015 that GWs were directly detected for the first time, by the GW observatory LIGO [28]. The event detected was a binary black hole merger, but this is not the only possible source of GWs. GW sources can be divided into two categories, that of cosmological sources, which include GWs created during the inflation and reheating epochs, along with GWs caused by phase transitions of the universe, and that of astrophysical sources, which include inspiral mergers and ringdown of compact binaries (white dwarfs, neutron stars, black holes) and the rotation of non-symmetric neutron stars [29].

3 THE MULTI-MESSENGER CONNECTION

This section will outline the theoretical reasoning behind pairing CRs and neutrinos in an analysis.

3.0.1 *Cosmic ray energy spectrum*

The CR energy spectrum follows a broken power-law, meaning that $\frac{dN}{dE} \propto E^{-\gamma}$. The few features of the spectrum indicate the points of transition from one value of γ to another. The main features, in the order of lowest to highest energy, are called 'the knee' at $E \approx 10^{15.6}$eV, 'the second knee' at $E \approx 10^{17.0}$eV, and 'the ankle' at $E \approx 10^{18.7}$eV. At low energies, the best-fitting γ value is $\gamma \approx 2.7$. The corresponding best-fit γ values in relation to the main features are as follows: from the knee to the second knee, $\gamma \approx 3.1$. From the second knee to the ankle, $\gamma \approx 3.3$. Finally, when reaching the ankle, the spectrum hardens again to $\gamma \approx 2.7$ (See Figure 3.1).

The origin of these features is a topic of much debate, and multiple explanations have been proposed. The most popular explanation for the two knees postulates that the decrease in flux pertains to the maximum attainable energies of different species of Galactic CRs. The primary acceleration engine for such high energy galactic CRs is thought to be SNRs. Using 'Hillas criterion' (introduced in the next subsection), one can then approximate the maximum energy attainable for such scenarios using typical values for core collapse SNe and the ISM, which roughly gives a maximum energy of $E_{max} \approx 10^{17}$eV, coinciding excellently with the second knee. This calculation is for iron nuclei - the maximum energy for protons under the same assumptions would be $E_{max,p} = E_{max,Fe}/26$. It is therefore quite satisfying that $E_{2knee}/E_{knee} \approx 25.1$. For this reason, the second knee is sometimes called the iron knee, to imply the maximum attainable energy of iron nuclei within the galaxy, while the first knee is simply the knee, having the same interpretation, but for protons [24, 8].

The reason behind the ankle is somewhat less clear. and several explanations exist. One postulates that the onset of a proton-dominated flux could account for the hardening. This explanation is somewhat controversial, however, since the two principal observatories investigating UHECRs disagree on the composition of CRs at these energies; the Pierre Auger Collaboration argues that their results indicate a transition to heavy nuclei, while the Telescope Array Collaboration argue that their data suggests a lighter compositon around these energies - however their findings are consistent with the more accurate Auger data. Another explanation is that of the onset of an extragalactic population of UHECRs with a harder spectrum. A possible scenario for such an explanation would be a situation wherein lower-energy CRs are magnetically confined within their acceleration engine. Slowly, a fraction of this population will photodisintegrate before it is accelerated to energies that allow escaping confinement. Some of the resulting secondary nuclei will be of lower charge, and thus no longer be magnetically confined to the region. Once the energy required to escape the magnetic confinement $E \approx E_{ankle}$ is reached, the spectrum naturally hardens again. Explanations of this category are powerful, as they not only provide a realistic scenario based on the current acceleration mechanism paradigm,

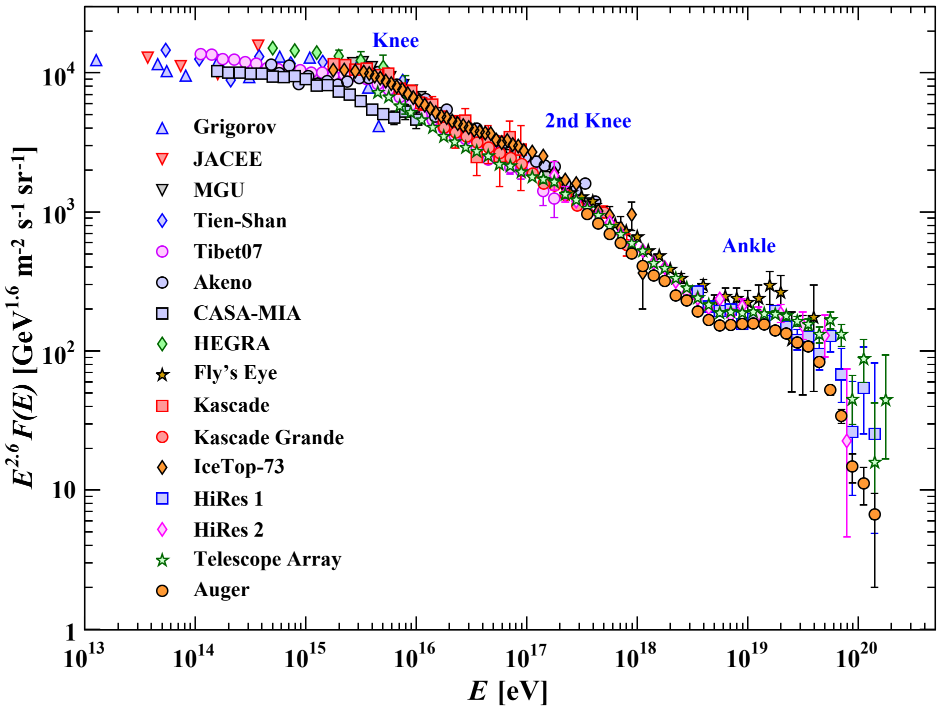

Figure 3.1: Cosmic ray all-particle energy spectrum with indications of the mentioned features of the spectrum. From Figure 29.8 of [30].

but they also provide an explanation for a lighter composition at $E_{2knee} \leq E \leq E_{ankle}$ reported by Auger [24, 8].

A final feature to point out is the end of the spectrum, caused by the GZK suppression effect (introduced later in this chapter) which affects UHECRs with energies at $\sim$ 50EeV and above.

3.0.2 *Ultra-high energy cosmic rays*

Ultra-high energy cosmic rays (UHECRs) are defined as cosmic rays with energies in excess of 10^{18}eV. As mentioned earlier, UHECRs are believed to be of extragalactic origin, the reason being threefold. Firstly, the sources within the galaxy are not thought to be energetic enough to be capable of accelerating CRs to ultra-high energies. Secondly, the observed UHECR events are largely isotropically distributed. If their origin was Galactic, one would expect a largely anistropic distribution of UHECRs, as the distance scales within the galaxy are too small to cause significant magnetic deflections. Lastly, the Larmor radius of such energetic particles would be larger than the size of the Milky Way, and thus the particles would escape into intergalactic space before reaching such high energies [31]. The Larmor radius argument can be used as a means of approximating the maximum attainable energy of a UHECR that is experiencing gradual acceleration while confined to some source region. This is exactly the nature of the principal candidate acceleration mechanism of UHECRs, called "first order Fermi acceleration" (introduced in detail in Section 3.1.1), which is a process in which CRs are accelerated by continously passing back and forth between the shock front of a strong shock. The approximation is made by starting from the expression for the Larmor radius $r_L = \frac{1}{\sqrt{4\pi\alpha}}\frac{E}{ZB}$, (with E being the particle's energy, Z being its charge and B being the magnetic field in which it propagates) and then demanding that the source region size R is at least of equal size to the Larmor radius r_L. This yields

$$E_{max} \approx \beta_s Z \left(\frac{R}{\text{kpc}}\right)\left(\frac{B}{\mu\text{G}}\right) 10^{18}\text{eV}, \tag{3.1}$$

where $\beta_s = V/c$ is the velocity of the shock front in units of c [32]. With this criterion, called the "Hillas criterion", one can use the magnetic field strength B and source region size R of known astrophysical objects to estimate which astrophysical sources could conceivably be capable of accelerating CRs to ultra-high energies. For comparison, one can infer the necessary radius of the LHC, should we want it to be capable of accelerating protons to GZK-cutoff energies at ~50EeV energies by setting $E_{max} = 5 \cdot 10^{11}$eV, $B = 10$T, $Z = 1$ and $\beta_s = 1$ (for simplicity). Using these values and isolating for R yields $R \approx 6 \cdot 10^7$km, which is about the size of the orbit of Mercury. Compiling these quantities and their variations for various known astrophysical objects allows one to make what is known as "the Hillas plot" (See Figure 3.2). As mentioned before, the few possible sources for UHECRs allowed by Hillas criterion include AGNs, GRBs and radio galaxy lobes.

3.0.3 *GZK effect*

At energies above $E > 5 \cdot 10^{19}$eV, protons will have Lorentz factors so high that they begin to lose energy by interacting with CMB photons, primarily through the $\Delta(1232)$-resonance and secondarily through resonances like the $\Delta(1620)$- and $\Delta(1700)$-resonances. This suppression effect is called the 'GZK-effect', named after it's discoverers, Greisen, Zatsepin and Kuz'min [3, 4], and it sets a soft 'GZK-limit' on observable UHECR energies. The pion production caused by the GZK effect lead to the following reactions:

$$\begin{array}{lllll} \gamma_{CMB} + p & \rightarrow & \Delta^+ & \rightarrow & n + \pi^+ \\ \gamma_{CMB} + p & \rightarrow & \Delta^+ & \rightarrow & p + \pi^0 \\ \gamma_{CMB} + p & \rightarrow & \Delta^{++} & \rightarrow & p + \pi^+ \end{array} .$$

The relative loss in energy for the proton per interaction is $\frac{\Delta E_p}{E_p} = 20\%$. The protons will also lose energy through pair production $\gamma_{CMB} + p \rightarrow p + e^+ + e^-$, but this effect is far less effective; at $E_p \approx 10^{19}$eV the energy loss length for pion production is $\sim$ 50Mpc while the energy loss length for pair production is $\sim$ 500Mpc. While heavier nuclei will not lose energy through pion production, they too will experience a severe suppression affect around the energy of GZK-suppression, as most γ_{CMB} photons will excite the giant dipole resonance, leading to photodisintegration (See figure 3.3). This limits the effective distance any UHECR with $E > 5 \cdot 10^{19}$eV could travel to the order of 100Mpc, as they would otherwise have

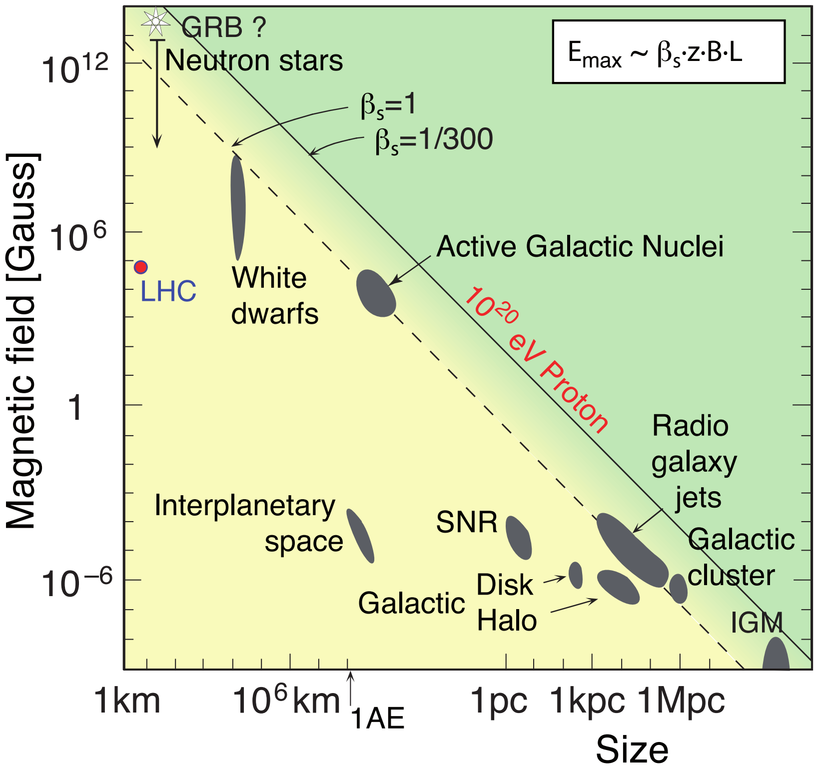

Figure 3.2: Hillas plot, showing possible sources of UHECRs. Dashed line corresponds the required B and R to accelerate a proton to 10^{20}eV with $\beta_s = 1$. From Figure 3 of [8].

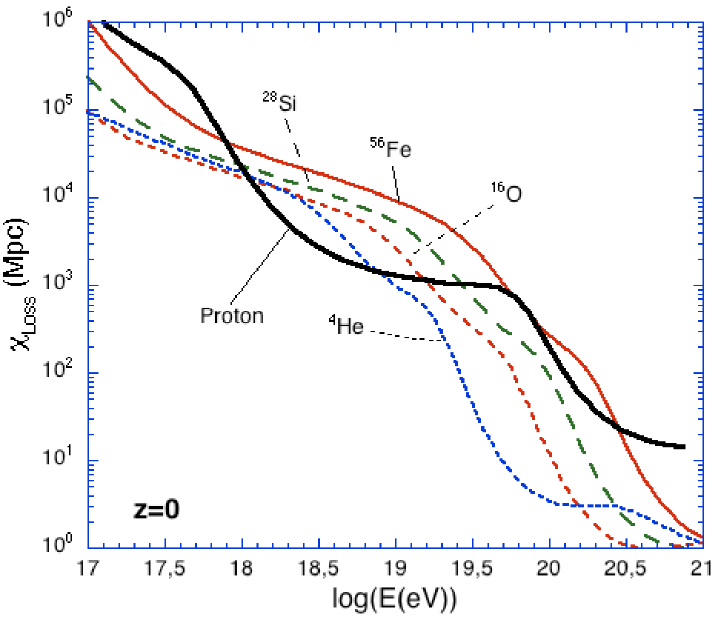

Figure 3.3: Energy loss lengths for various UHECR nuclei as a function of total energy, evaluated at $z = 0$. From Figure 1c of [8].

been attenuated out of the GZK-energy regime [3, 4, 24, 31]. This effect proves to be essential in pinpointing UHECR point sources, as the limit on propagation distance can be translated into a limit on the degree to which a UHECR has been magnetically deflected. Depending on the nuclei and the input parameters for the magnetic fields a UHECR is subjected to, the expected deflection comes down to somewhere between $3 - 30$ deg in low-deflection scenarios (See Section 4.4 for more details), which means it could be possible to gain insight into UHECR source locations through statistical analysis of large sets of UHECR data. So far, however, no such analysis has yielded any conclusive evidence for a UHECR source, which is in large part due to the scarcity of CRs with $E > 50$EeV; a common statement made to emphasize the difficulty of detecting these particles is that at $E > 100$EeV, less than one particle is expected per km^2 per century [8]. As a final note, the GZK effect is also predicted to result in a flux of extremely high energy neutrinos, stemming from the decay of the pions associated with the $\gamma_{CMB} + p$ interactions. As of yet, however, no cosmogenic neutrinos have been conclusively identified [33].

3.1 *UHE cosmic ray multi-messenger connections*

In order to understand how UHECRs are linked to other multi-messenger particles, it is important first to introduce the UHECR acceleration mechanism, and the environment in which they are accelerated. Firstly, it is prudent to note that there is not simply a single model explaining how UHECRs are created. UHECR origin models can roughly be divided into two main categories: acceleration models, wherein UHECRs are accelerated to ultra-high energies by a magnetic field, and more exotic models, for instance 'top-down' models. These models postulate that UHECRs stem from the decay of new super-heavy particles, or from topological defects [8]. We shall only consider the former in this thesis. The acceleration models can once again be divided into two categories - 'one-shot' models wherein the particle is accelerated in a single instance, and Fermi acceleration wherein the particle is accelerated through several random encounters [24]. Two preliminary criteria a UHECR acceleration canditate must fulfill is that a plausible acceleration mechanism is present, and the aforementioned Hillas criterion, which demands thats the Larmor radius corresponding to a CR at a given energy is equal to or less than the size of the accelerator region. These two criteria by themselves are not necessarily enough to qualify a potential accelerator candidate, but they remain effective ways of easily disregarding a lot of potential sources of UHECR's. For instance, Hillas criterion overlooks the effect of energy losses during acceleration, meaning that while shocks stemming from structure formation, with $B \approx 10^{-6}G$ and $R \approx 1$Gpc technically fulfill the criterion, the acceleration process would be too slow to allow for the acceleration up to UHECR energies. In the reference [24], the general constrains on UHECR accelerators are summarized as follows:

- The source region must be able to contain the particles during acceleration
- The source must have sufficient energy to transfer to the particles during acceleration
- The particles' interaction losses must not exceed or equal the energy gained during acceleration
- One must be able to approximately recover the observed UHECR flux using the power and density of the sources.
- One must be able to approximately recover the observed UHECR energy spectral index from the acceleration mechanism of the source.
- Accompanying radiation from the source must not exceed the observed flux for neither a given source nor the diffuse background.

That leaves the question of energy injection. The traditional model for CRs gaining energy is that of diffusive shock acceleration at the shock front of e.g. a supernova remnant (SNR), a process which we will now introduce.

3.1.1 *Fermi acceleration*

The primary acceleration mechanism candidate for UHECR's is known as first order Fermi acceleration (also called diffusive shock acceleration), which is a variant of second order Fermi acceleration. Fermi presented his idea of second order Fermi acceleration in 1949 as a possible mechanism for generating CRs [34]. One of the primary strengths of the model stems from its ability to reproduce a CR power-law energy spectrum. In essence, the model hypothesized CRs having stochastic encounters with interstellar clouds propagating with some random velocity V. These clouds would function as magnetic mirrors, and over many such encounters, the CR would gain energy. Fermi showed that on average, the particle would experience a relative increase in energy given by $\frac{\Delta E}{E} \propto \left(\frac{V}{c}\right)^2$. The mechanism is called second order Fermi acceleration exactly due to the exponent in the relative energy increase. Furthermore, Fermi showed that the corresponding energy spectrum would

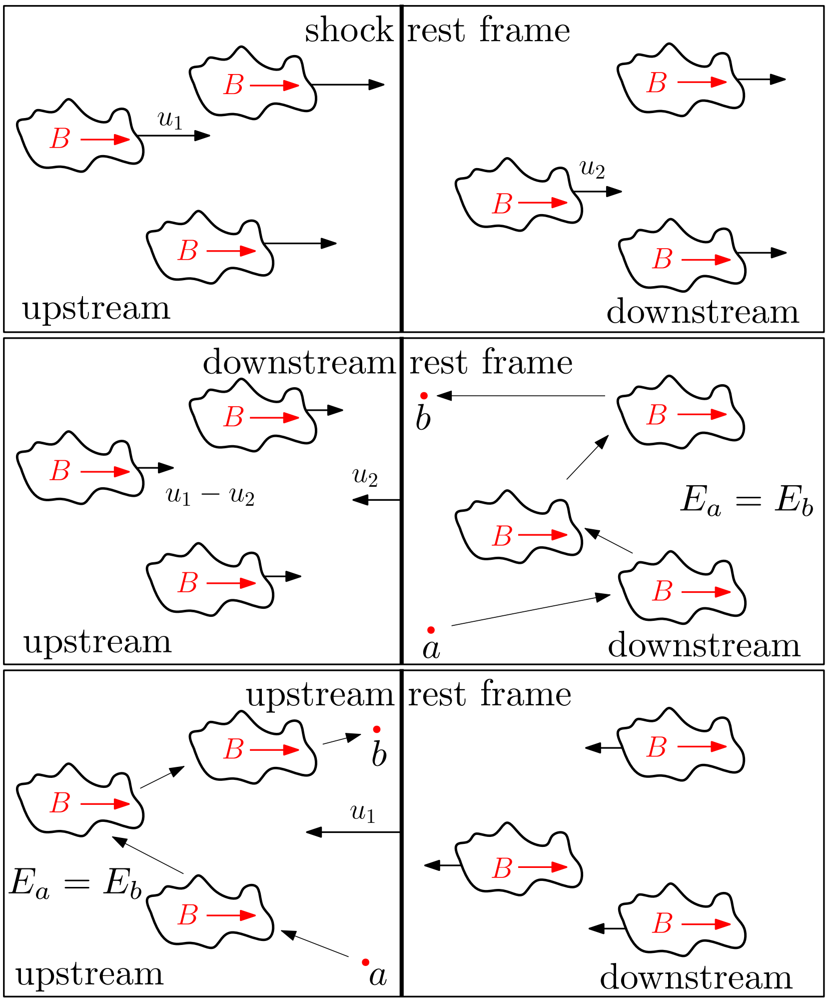

Figure 3.4: Schematic overview of first order Fermi acceleration. Here $u_1 = U$ and $u_2 = \frac{1}{4}U$. The 'blobs' are groupings of plasma with a specific peculiar velocity and some magnetic field B. Also included is how some charged particle (red dot) could scatter from the magnetic fields and thus be directed through the shock front. From Figure 12 of [24].

be given by a power-law with spectral index $\gamma = 1 + (\alpha\tau_{esc})^{-1}$, where α is the rate of energy gain and τ_{esc} is the characteristic escape time for a CR in the system. Unfortunately, the model has several issues, primarily that in most cases, the mechanism would be extremely slow in accelerating CRs to high energies, as galactic interstellar clouds have low velocities relative to c, $\frac{V}{c} \leq 10^{-4}$, and as CRs only interact with a few clouds per year. Additionally, there is no obvious reason why the spectral index predicted by the model should equal that of the observed CR spectral index.

The core idea of the mechanism, namely that of the 'magnetic mirrors' was revitalized in the late '70s when it was shown that strong shock fronts could create a similar environment of magnetic mirrors that was seen in the original Fermi model [35].

Imagine a shock front propagating with some nonrelativistic velocity U. On one side of the shock is the unshocked upstream region, and on the other is the shocked downstream region. For an observer within the upstream frame of reference, it will appear as though the shock front is moving towards them with a velocity U, and as though the downstream fluid approaches with a velocity $V = \frac{3}{4}U$ (general result for idealized shocks). For an observer within the downstream frame of reference, the shock front is moving away from them with a velocity $\frac{1}{4}U$ while the upstream fluid approaches with a velocity $V = \frac{3}{4}U$. Thus no matter the side of the shock you are on, it appears as though either side is approaching you with $V = \frac{3}{4}U$. If we then imagine some particle in the upstream frame of reference with energy E crossing the shock front to the other side and then isotropizing by effectively elastically scattering through interactions with the magnetic fields of the plasma, we can calculate the energy it gains from each crossing. So, if a particle with energy E starts upstream and crosses the shock front, its energy in the downstream region can be calculated through

$$E' = \gamma_V \left(E + p_x V\right), \tag{3.2}$$

where γ_V is the Lorentz-factor of the shock front, and where we have assumed that the x-coordinate is perpendicular to the shock front for the sake of simplicity. Since the particle is relativistic, we have that $p_x = (E/c)\cos\theta$ (where θ is the angle with which the particle passes through the shock front) and $E = pc$, and since the shock is nonrelativistic, we have that $\gamma_V \approx 1$. We then obtain:

$$\Delta E = E' - E = \gamma_V \left(E + p_x V\right) - E = \left(E + p\cos\theta V\right) - E = pV\cos\theta. \tag{3.3}$$

Giving us the following expression for the relative increase in energy for the crossing:

$$\frac{\Delta E}{E} = \frac{V}{c}\cos\theta. \tag{3.4}$$

As stated earlier, there is no effective difference between crossing from upstream to downsteam and vice versa, and so the above expression is also true for a particle crossing from downstream to upstream. One can then calculate the average energy for each crossing by using that the probability of a given entry angle between θ and $\theta + \mathrm{d}\theta$ is given by $p\left(\theta\right) = 2\sin\theta\cos\theta\mathrm{d}\theta$:

$$\left\langle \frac{\Delta E}{E} \right\rangle = 2\frac{V}{c}\int_0^{\pi/2} \sin\theta\cos^2\theta\mathrm{d}\theta = \frac{2}{3}\frac{V}{c}. \tag{3.5}$$

Since this result is the average energy gain per crossing, the average energy gain for a full cycle would be $\frac{4}{3}\frac{V}{c}$. From here, we can make a simple calculation to find the corresponding energy spectrum of CRs accelerated by such a mechanism. Firstly, we point out that in this idealized system, particles will not escape upstream, as they will scatter with Alfvén waves and effectively isotropize within the upstream region's frame of reference, thus eventually the shock front should catch up to the particles. There is only a probability of escape through advection in the downstream case. We now define $E = E_0\beta^k$ as the average energy of a particle after k cycles, and $N = N_0 P^k$ as the number of particles remaining after k cycles, where the subscript 0 denotes the initial energy/number of particles, β is the relative increase in energy per cycle and P is the probability to avoid escaping per cycle. From these two equations, one can then obtain:

$$\frac{N}{N_0} = \left(\frac{E}{E_0}\right)^{\ln P/\ln\beta}. \tag{3.6}$$

As some of the N particles reaching this energy will undergo more cycles without escaping, we have the energy spectrum given by

$$\frac{N(E)}{\mathrm{d}E}\mathrm{d}E = C \cdot E^{-1+\ln P/\ln\beta}, \tag{3.7}$$

where C is some constant. One can then show that the fraction of particles lost to advection is given by U/c, where U is the velocity of the shock front relative to the upstream region. Thus, we have that $P = (1 - U/c)$ and $\beta = \left(1 + \frac{4}{3}V\right) = \left(1 + \frac{4}{3}\frac{3}{4}U\right) = (1 + U)$. We then obtain

$$\ln P/\ln\beta = -1 \Rightarrow \frac{N(E)}{\mathrm{d}E}\mathrm{d}E = C \cdot E^{-2}. \tag{3.8}$$

We have now obtained a power-law with $\gamma = 2$ from this relatively simple approach. While this does not exactly match the spectral indices from the observed *CR* flux, one must bear in mind that this is a highly idealized model, and reality will be more complicated than presented here. The model's strengths are its roughly accurate prediction for the value of γ and its ability to explain why various astrophysical processes and objects would be capable of all producing CRs with the same power-law energy spectrum [36, p. 564-572].

3.1.2 *Photon and neutrino as products of CR interactions*

Assuming the scheme of Fermi acceleration is correct, or at least approximately correct, then CR acceleration is a long and arduous process, and one that takes place in environments with a multitude of high-energy particles capable of interacting with each other. For this reason, it is expected that any flux of high-energy CRs should be accompanied by a flux of both photons and neutrinos. These secondaries are produced through proton-proton processes, and the same proton-photon processes seen in the GZK-effect, though in this scheme the CRs interact with high-energy photons rather than CMB photons. The dominant neutrino channels in the proton-proton processes are [31]

$$\begin{aligned} p + p &\rightarrow p + p + \pi^0, \\ p + p &\rightarrow p + n + \pi^+. \end{aligned}$$

The same processes occur for neutrons (that stem from the proton-photon processes also present within the source region) as well, yielding π^- particles as well. These charged pions decay into neutrinos

$$\begin{aligned} \pi^+ &\rightarrow \mu^+ + \nu_\mu \rightarrow e^+ + \nu_e + \bar{\nu}_\mu + \nu_\mu, \\ \pi^- &\rightarrow \mu^- + \bar{\nu}_\mu \rightarrow e^- + \bar{\nu}_e + \nu_\mu + \bar{\nu}_\mu. \end{aligned}$$

with the individual neutrinos receiving $\sim 5\%$ of the progenitor proton's energy. The neutral pions decay into photons

$$\pi^0 \rightarrow \gamma + \gamma\ .$$

with the photons each getting 1/2 of the parent pion energy, which in turn receives $\sim 20\%$ of the parent CR energy. These proton-proton and proton-photon processes are thought to take place through interactions of CRs with ambient molecular clouds and radiation fields respectively at the source region, and since neither neutrinos nor photons are magnetically deflected, the initial thought is that one should easily be able to resolve UHECR sources through observation of these secondaries. Unfortunately, the situation is more complicated in the case of both photons and neutrinos. Secondary photons stemming from UHECRs would have energies well above the TeV range, to which the universe is quite opaque: the absorption length D for photons at energies between 10^{14}eV and 10^{19}eV is $D \leq 1$Mpc. This is due to e^+e^- pair production through interaction with the CMB. Additionally, high-energy gamma-rays can be created in purely leptonic processes, further complicating any potential analysis [37, 10].

Neutrinos, however, can only originate from hadronic processes, and thus the arrival directions of any high-energy neutrino flux should correlate with the arrival directions of a high-energy CR flux. As neutrinos receive roughly $\sim 5\%$ of the progenitor proton's energy, we might expect to observe neutrinos with $E = 100\text{PeV} - 1\text{EeV}$ from the source. Alas, no such neutrinos have been detected. The most energetic neutrinos observed have been detected by IceCube, and have energies at the order of a couple of PeV, several orders of magnitudes below the energies related to GZK-suppressed UHECRs [12]. Thus, attempting to infer source locations by correlating between these neutrinos and the CRs of corresponding energy might seem like a lost cause, as the sub-GZK CRs could have arbitrarily large deflections, or might diffuse before they ever arrive at the Earth, and indeed it is.

It turns out, however, that it has proven possible to model scenarios wherein an acceleration region of UHECRs is magnetically confining all but the most energetic CRs, effectively creating a flux of secondaries upto a critical energy where the CRs begin to escape magnetic confinement in accordance with the principles of the Hillas criterion. Such a mechanism could result in a disjoint between UHECR and neutrino energies, in spite of a shared point of origin. In fact, the observed astrophysical flux from IceCube has been compared the predictions of various acceleration regions for UHECRs, including AGNs and GRBs, and some predictions have been found to be consistent with the observed flux [38]. In addition, there are no clear anisotropies within the bulk of the observed astrophysical neutrinos. This alludes to the fact that the neutrinos primarily have an extragalactic origin. This notion is supported by the nonobservation of a high-energy gamma-ray flux corresponding to the observed neutrino flux. Such gamma-rays should be able to travel Galactic distances, and thus any source emitting them within our Galaxy should be visible. Furthermore, the observed neutrino flux also approximately corresponds to an upper limit for neutrinos produced in UHECR sources [9].

It should be mentioned that none of the abovementioned observations guarantee that the astrophysical neutrino flux stems from sources of UHECRs. These may be coincidental, and indeed, explanations independent of UHECR sources do exist [38]. That being said, they provide ample justification for attempting a correlation between UHECRs and high-energy neutrinos. With this in mind, the stage seems to be set for attempting to usehigh-energy neutrinos to identify UHECR sources. It must be added that neutrinos, with their extremely large mean free paths, are capable of reaching the earth from sources at high redshifts. Thus, a large fraction of observed high-energy neutrinos might truly be uncorrelated with any observable source of GZK-suppressed UHECRs, as any such source would be constrained to lie within local space. Furthermore, detection of such high-energy neutrinos is a recent achievement in neutrino astronomy, and consequently the data sample at very high energies is still small.

4 METHOD: THEORY

In this section, a generalized mathematical framework for distributing high energy neutrino and UHECR events in an expanding universe will be introduced. First, a brief introduction to the relevant cosmology is given. Then the distribution of sources will be presented. Then a means of evaluating the flux contribution from each source given a fixed amount of observed particles will be introduced. Afterwards, an introduction to the magnetic fields affecting CRs propagating both inside the Milky Way and in intergalactic space. Lastly a brief introduction to the statistical methodology is given.

4.1 *ΛCDM cosmology*

It has been known for many years that the universe is expanding, with the expansion scaling with distance. This effects results among other things in an observable redshift z of light from distant sources, and must be taken into consideration when calculations pertain to the propagation of particles over cosmological distances. As neutrino sources could hypothetically be at very high redshifts, using a cosmological framework that takes into account the non-Euclidian nature of an expanding universe becomes important. The framework used in this thesis is that of ΛCDM cosmology, which posits that the the universe primarily consists of matter, cold dark matter (CDM) and a cosmological constant Λ. The primary variable in the framework is the Hubble parameter $H(z)$, denoting the expansion of the universe at redshift z, parametrized in ΛCDM by

$$H(z) = H_0 \sqrt{\Omega_{rad}(1+z)^{-4} + (\Omega_{CDM} + \Omega_b)(1+z)^{-3} + \Omega_k (1+z)^{-2} + \Omega_\Lambda} \quad (4.1)$$

where H_0 is $H(0) \approx 67.74 \mathrm{km\,s^{-1}Mpc^{-1}}$ [39], and the Ω's denote the energy density fractions of the different components of the universe, being baryonic matter Ω_b, dark matter Ω_{CDM}, radiation Ω_{rad} (which is very small and thus generally ignored), and dark energy Ω_Λ. The distance measures relevant to the calculations in this thesis is the comoving distance, luminosity distance and light travel distance [40]. The comoving distance d_C relates the distance to an object at redshift z the current time. The luminosity distance d_L is relates to an object's bolometric flux and bolometric luminosity. The light travel distance d_{LTD} corresponds to the total distance traveled by a particle moving with velocity c from a source at redshift z to the observer.

The comoving distance is given by

$$d_C(z) = c \int_0^z \frac{\mathrm{d}z'}{H(z')} \quad (4.2)$$

the luminosity distance is given by

$$d_L(z) = (1+z)\, d_M(z) \quad (4.3)$$

and the light travel distance is given by

$$d_{LTD}(z) = c \int_0^z \frac{\mathrm{d}z'}{(1+z')\, H(z')} \quad (4.4)$$

4.2 *Source distribution*

The distribution of sources has two 'components' to it, the redshift component and the angular component. The redshift distribution of sources is estimated through evaluation of the star-formation rate (SFR) at a given redshift under the assumption that any source candidate approximately follows the same redshift evolution as the number density of stars. SFR can be approximated as a simple piecewise function of redshift given by

$$\rho\left(z, \rho_0\right) = \rho_0 \left(1+z\right)^{n_i}, \tag{4.5}$$

with

$$n_i = \begin{cases} 3.4 & \text{for } z < 1 \\ -0.3 & \text{for } 1 \leq z < 4 \\ -3.5 & \text{for } 4 \leq z \end{cases}, \tag{4.6}$$

and ρ_0 being the source density in our local universe [41].

The angular distribution of sources is assumed to be isotropic. It should be noted that a more realistic approach to the problem of source distribution could be to use one of the new estimations of the large-scale structure density distributions of the local universe [42], however this was not implemented due to time constraints. Finally, the total number of expected sources within a sphere denoted by its radius in redshift z is calculated using the expression

$$N_{sources} = \int_0^z \frac{\mathrm{d}V_c\left(z\right)}{\mathrm{d}z'} \rho\left(z'\right)\, \mathrm{d}z' = c \int_0^z \frac{1}{H\left(z'\right)} 4\pi d_C \left(z'\right)^2 \rho\left(z', \rho_0\right)\, \mathrm{d}z', \tag{4.7}$$

where V_c is the comoving volume, given by $\frac{4}{3}\pi d_c^3$.

4.3 *Source flux/luminosity calculation*

In this section we will derive an expression for the total number of particles observed from a source at a certain redshift, given a source density and total number of particles observed. Calculating the flux is done under a set of assumptions. First and foremost, it is assumed that all sources share the same emission rate, meaning for instance that a source at $z = 3$ emits as many high-energy neutrinos per second as a source at $z = 0.05$. Furthermore, it is assumed that the sources emit neutrinos and UHECRs with a fixed power-law spectrum for each of the particles. Starting from this general principle, with some arbitrary particle species, we have

$$Q\left(E\right) = Q_0 \left(\frac{E}{E_0}\right)^{-\alpha}, \tag{4.8}$$

where $Q\left(E\right)$ is the emission rate as a function of particle energy, E_0 corresponds to some normalization energy, Q_0 corresponds to the emission rate at the normalization energy, and α being the power-law index. Furthermore, the diffuse flux of the particle originating in multiple sources is given by [43]

$$\phi\left(E\right) = \frac{c}{4\pi} \int_0^\infty \frac{\mathcal{L}\left(z, \left(1+z\right)E\right)}{H\left(z\right)}\, \mathrm{d}z, \tag{4.9}$$

where $\mathcal{L}(z,(1+z)E) = Q((1+z)E)\rho(z,\rho_0)$. This means that the diffuse flux can be expressed as a function of energy through:

$$\phi(E) = \frac{c}{4\pi} Q_0 \left(\frac{E}{E_0}\right)^{-\alpha} \int_0^\infty \frac{\rho(z)}{H(z)} (1+z)^{-\alpha} \; \mathrm{d}z. \tag{4.10}$$

In turn, the spectral flux of a point source ϕ_{PS} at redshift z would be given by the following equation

$$\phi_{PS}(E,z) = \frac{Q((1+z)E)}{4\pi d_L^2} (1+z)^2 \tag{4.11}$$

The total expected energy flux from this source is then given by

$$\lambda_{PS,E}(z) = \int_0^\infty E\phi_{PS}(E,z) \; \mathrm{d}E \tag{4.12}$$

So, if we insert, we obtain:

$$\lambda_{PS,E}(z) = \frac{1}{4\pi d_L^2} \int_0^\infty E(1+z)^2 Q((1+z)E) \; \mathrm{d}E \tag{4.13}$$

It is using this equation that we justify the additional factor of $(1+z)^2$ to $\phi_{PS}(E,z)$, see Appendix A.1. If, instead, we are only interested in the total particle flux observed, we remove the factor of E (not a mathematical operation, we are just not interested in scaling with the energy) from within the integral, and using the power-law definition of $Q(E)$, we obtain:

$$\lambda_{PS}(z) = \frac{1}{4\pi d_L^2} \int_0^\infty Q_0 (1+z)^2 (1+z)^{-\alpha} \left(\frac{E}{E_0}\right)^{-\alpha} \; \mathrm{d}E = \frac{Q_0 (1+z)^{2-\alpha}}{4\pi d_L^2} \int_0^\infty \left(\frac{E}{E_0}\right)^{-\alpha} \; \mathrm{d}E \tag{4.14}$$

This equation gives us the particle flux from the source at Earth. To obtain total number of particles observed over an observational period with some detector, we multiply with the detector's effective area and the time it's been live, and the expression becomes:

$$\lambda_{PS,tot}(z) = T_{live} \frac{Q_0 (1+z)^{2-\alpha}}{4\pi d_L^2} \int_0^\infty A_{eff}(E,\Omega) \left(\frac{E}{E_0}\right)^{-\alpha} \; \mathrm{d}E \tag{4.15}$$

Where the effective area depends on both the part of the sky Ω that we're observing as well as the energy E of the flux. For simplicity, we will assume that we're fully sensitive to any particles above a certain threshold energy E_{th}, so that $A_{eff}(E,\Omega) \to A_{eff}(\Omega)\Theta(E - E_{th})$ where $\Theta(x - x_0)$ is the Heaviside step-function. This alters the expression to become:

$$\lambda_{PS,tot}(z) = A_{eff}(\Omega) T_{live} \frac{Q_0 (1+z)^{2-\alpha}}{4\pi d_L^2} \int_{E_{th}}^\infty \left(\frac{E}{E_0}\right)^{-\alpha} \; \mathrm{d}E \tag{4.16}$$

The number of particles $\lambda_{PS,tot}(z)$ from a source at redshift z can then be related to the total expected number of particles N_ν observed from all sources through either of the two integrals

$$N_\nu = \int_0^\infty \lambda_{PS,tot} \frac{\mathrm{d}N_{source}}{\mathrm{d}\lambda_{PS,tot}} \,\mathrm{d}\lambda_{PS,tot} = \int_0^\infty \lambda_{PS,tot}\left(z\right) \frac{\mathrm{d}N_{source}}{\mathrm{d}z} \,\mathrm{d}z \tag{4.17}$$

We now go back to Equation 4.10, which is the expression for the diffuse flux. We can remove the factor of $\frac{1}{4\pi}$ to remove the unit of sr^{-1}, so instead we have the flux from the whole sky. Then, the equation can be related to the total number of observed particles of species x N_x through

$$N_x = T_{live} A_{eff} \int_{E_{th}}^\infty \phi\left(E\right) \,\mathrm{d}E \tag{4.18}$$

Thus

$$N_x = c T_{live} A_{eff} Q_0 \int_0^\infty \frac{\rho\left(z\right)}{H\left(z\right)} \left(1+z\right)^{-\alpha} \,\mathrm{d}z \int_{E_{th}}^\infty \left(\frac{E}{E_0}\right)^{-\alpha} \,\mathrm{d}E \tag{4.19}$$

One can now define the following two quantities $\zeta = \int_{E_{th}}^\infty \left(\frac{E}{E_0}\right)^{-\alpha} \,\mathrm{d}E$ and $\xi = \int_0^\infty \frac{\rho(z)}{H(z)} \left(1+z\right)^{-\alpha} \,\mathrm{d}z$, and then solve for Q_0 to obtain:

$$Q_0 = \frac{N_x}{T_{live} A_{eff}} \frac{1}{c} \frac{1}{\xi\zeta} \tag{4.20}$$

Then, by inserting Equation 4.20 into 4.16, we obtain

$$\lambda_{PS,tot}\left(z\right) = \frac{N_x}{T_{live} A_{eff}} \frac{1}{c} \frac{1}{\xi\zeta} A_{eff} T_{live} \frac{\left(1+z\right)^{2-\alpha}}{4\pi d_L^2} \zeta = \frac{N_x}{4\pi d_L^2} \frac{\left(1+z\right)^{2-\alpha}}{c\xi} \tag{4.21}$$

and have thus made the expression independent of the live time T_{live}, the effective area A_{eff} and the energy integral ζ. This expression allows evaluation of the expectation flux from a source at redshift z given a total number of observed particles N_x with some power-law spectrum characterised by α, and the integral $\xi = \int_0^\infty \frac{\rho(z)}{H(z)} \left(1+z\right)^{-\alpha} \,\mathrm{d}z$ which normalizes the flux based on the evolution of sources in redshift, and must be numerically calculated.

4.4 *Magnetic deflection of CRs*

Magnetic fields are ubiquitous in the universe, and are seen on all scales. Thus, propagating CRs will be subject to constant magnetic deflection, with some deflection being caused by regular magnetic fields, and some by random magnetic fields. In this section, first the approach used to calculate the deflection of a CR that is propagated through random magnetic fields will be described. Next, an introduction to the two 'types' of magnetic fields considered in this thesis is given, namely the Galactic magnetic field, and the extragalactic magnetic field.

4.4.1 *Estimating the effect of random magnetic fields*

Any CR propagating through space will be affected by a multitude of magnetic fields, all with their own orientations. Thus, it's important to be able to calculate the average deflection expected for a CR emitted by a source at distance D. The scenario is as follows: Consider a space with a series of magnetic fields each with a correlation length λ, within which the magnetic field's orientation is constant. As one moves from one magnetic field to another, the orientation is randomized until another length $L = \lambda$ is traversed, and a new magnetic field is entered. For simplicity, these magnetic fields are all assumed to have the same magnetic field strength B. Then, for a particle with energy E and electric charge $Z = 1$, the expectation displacement is given by [44]

$$\theta_s{=}0.025^\circ(\frac{D}{\lambda})^{1/2}(\frac{\lambda}{10\text{Mpc}})(\frac{B}{10^{-11}\text{G}})(\frac{E}{10^{20}\text{eV}})^{-1} \tag{4.22}$$

4.4.2 *The Galactic magnetic field*

The Galactic magnetic field (GMF) is composed out of regular and random magnetic fields. Due to its importance in e.g. CR physics, the GMF has been extensively studied. Unfortunately, the presence of the random components makes the GMF exceedingly difficult to accurately model. With that being said, it is not a completely lost cause, and attempts at modelling the GMF in its entirety exist (e.g. [6]), though the models are still incomplete. The hope then, is that one day the regular field will be well enough reconstructed to make the random component the only source of error from the GMF on the arrival direction of CRs. Thus, we abandon what at the current time seems a difficult task and ignore any regular component to the GMF and instead focus on the random component of the GMF (rGMF) instead. The rGMF has two primary components, one isotropic and one anistropic, both with B values of the order of $1 - 10\mu$G. Work has been done to estimate the possible displacement effect caused by the rGMF on UHECRs, and it has been found that the expected displacement is around $1^\circ - 2^\circ$ for most arrival directions, save for UHECR's moving through the Galactic plane, where the expected displacement reaches around 5°. This is model dependent, however, and instead, a simplified approach is chosen: as best-fit rGMF component B-values tend to lie around $1 - 10\mu$G, and as the correlation length of random magnetic fields in the galaxy are of the order of $\sim$ 220pc or above[45], we instead estimate the displacement caused by the rGMF through Equation 4.22, setting $D = 7$kpc, corresponding to Galactic distance scales, and finding for a 60EeV proton that $\theta_{s,rGMF} \approx 2.6^\circ$, which is in agreement with the findings of [46].

4.4.3 *The extragalactic magnetic field*

The extragalactic magnetic field (EGMF) refers to extremely weak magnetic fields that are omnipresent, even in the voids of Large Scale Structure (LSS). The origin of these fields could be primordial, but remains uncertain [47]. As these fields should be extremely weak, with upper bounds on B being of the order of 1nG, knowledge of them is somewhat scarce. Thus, the scale at which they are coherent λ, and their actual magnetic field strength are still unknown. The parameter space of allowed values for B and λ is very large, with $B = 10^{-15} - 10^{-9}$ G and $\lambda = 10^{-7} - 10^4$ Mpc being the allowed range based on early Universe generation mechanisms and observational bounds [7]. This range may be tightened by adding a variety of other bounds from e.g. Fermi telescope and theoretical/simulation bounds, though we will refrain from doing so.

Using the range of possible values listed above with Equation 4.22, the possible deflection angles caused by the EGMF for a 60EeV proton that has propagated $D = 100$Mpc range from no zero deflection ($\theta_s \approx 0$) to complete randomization of observed arrival direction ($\theta_s > 360$). Rather than consider this full range of possibilities, we will constrain ourselves to considering two cases, one wherein the EGMF is the dominant field between the GMF and the EGMF for particles having propagated 300Mpc or less, and one wherein the rGMF is dominant instead. Consequently, two combinations of B and λ were selected for the EGMF on an ad hoc basis to provide the values $\theta_{s,EGMF} + \theta_{s,rGMF} \approx 3^\circ$ and $\theta_{s,EGMF} + \theta_{s,rGMF} \approx 30^\circ$.

4.5 *Statistical tools*

This subsection will briefly introduce the notion of the test statistic and how they are utilized in hypothesis testing.

4.5.1 *Test statistics*

Among the most import mathematical methods used in physics is statistical hypothesis testing, wherein one uses statistics to make quantitative statements about the validity of a theory (called the signal hypothesis H_1) based on experimental data. The methodology involves comparing the relation between the experimental data and the signal hypothesis as an alternative to a null hypothesis H_0 (also called the background hypothesis), which states that there is no relation between the experimental data and H_1. This comparison is made by analysing the properties of a quantity called the test statistic (TS), which is an arbitrary quantity that is derived from one's data sample. While a TS can be defined in any number of ways, traits such as fast calculability and well-known behavior are desirable. The most important feature of a TS however, is that it produces clearly seperated TS-value distributions given either H_1 or H_0.

4.5.2 *Sensitivity and upper limit*

The main statistical criterion utilized in this thesis will be that of the 90% sensitivity level, which is defined through the degree to which two TS distributions, one from signal and one from background, are seperated. We have reached the 90% sensitivity level if 90% of the signal TS values are equal to or greater than the median of the background TS value. See Figure 4.1 for an example. From this plot, it should be clear that reaching the 90% sensitivity level is not the same as guaranteeing a significant result. Mathematically, this concept can easily be explained. Say the background TS, TS_B, has the probability density function $p_0\left(TS_B\right)$, and similar for the signal we have $p_1\left(TS_S\right)$. The probability that a scenario with no signal would produce a TS_B value of TS or greater is then given by $\alpha = \int_{TS}^{\infty} p_0\left(TS_B\right) \mathrm{d}TS_B$, called the statistical significance, and the probability that a scenario with a signal would produce a value TS_S of TS or less is given by $\beta = \int_{\infty}^{TS} p_1\left(TS_S\right) \mathrm{d}TS_S$, where $1 - \beta$

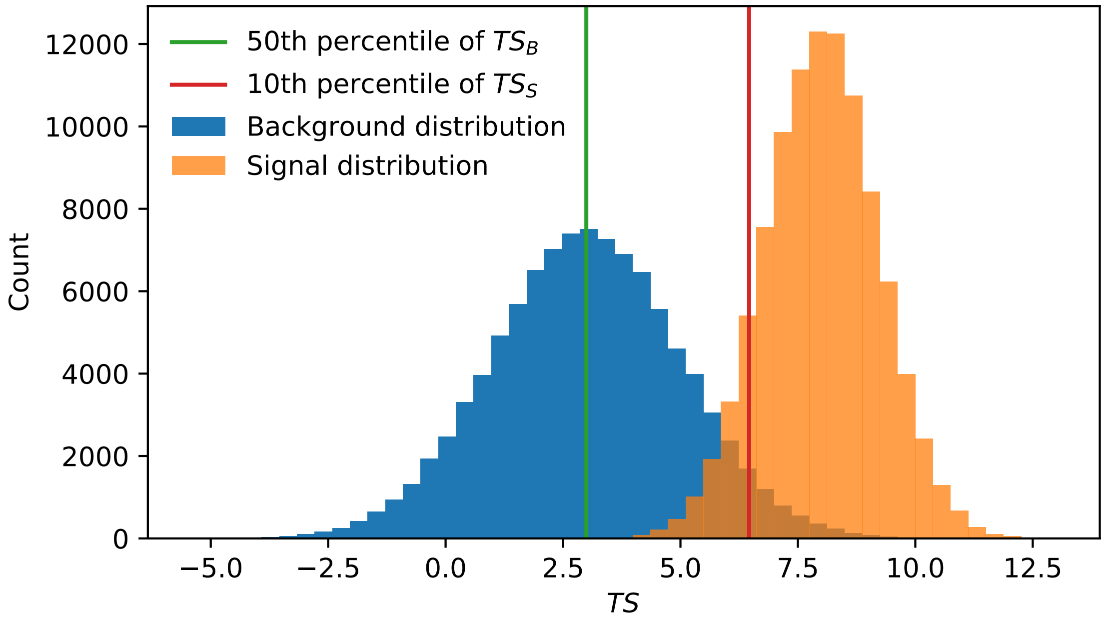

Figure 4.1: Example of sensitivity concept using two Gaussians - as $TS_{B,50} < TS_{S,10}$, we conclude that we are sensitive in this case.

is called the statistical power. The 90% sensitivity level is then the situation defined as $\alpha = 0.5$ and $\beta = 0.1$.

In the case with actual data, instead of evaluating the sensitivity, the upper limit on the TS is calculated. If a value TS_{data} is evaluated, this is then done using $\alpha = \int_{TS_{data}}^{\infty} p_0\left(TS_B\right) \mathrm{d}TS_B$ and $\beta = 0.1$. As the density of sources will be inversely proportional to TS, an upper limit on the TS translates into a lower limit on the density.

5 METHOD: IMPLEMENTATION

This chapter will describe the computer implementation used for the project. First an overview will be given of the primary code, along with descriptions of the individual modules. Furthermore, the most important of the various approximations made during the implementation will also be mentioned and justified. Then, typical simulation results will be showcased and briefly explained. Finally, a variety of consistency checks to ensure that the simulation is working as expected will be showcased as evidence for a correct implementation of the physics of the problem.

5.1 *Overview of code*

The purpose of the code is to produce sets of background and signal data from realizations based on realistically motivated physical input parameters. The principal data output is in the form of a test statistic, everything else is related to diagnostics in some way. Introductions to the various TS's evaluated for each of the analyses are given in their respective chapters. First we will describe the process of how a realization is made, and how a TS value is produced in general. After, we will describe some of the key differences between the neutrino and CR implementations. Finally we will present an overview of the various simulation variables used in the implementation.

5.1.1 *General approach*

The general implementation is largely modular, and for that reason it is simple to describe the individual main steps seperately. First, a set of input parameters are passed to the function. These input parameters include the local source density ρ_0, the total number of observed particles N and other quantities pertaining to particle-specific simulations such as the neutrino signal-to-background ratio, the UHECR energy etc. The code then uses these input parameters to produce a 'skymap' - a pixelized projection of the celestial sphere - with neutrino and CR events. These event distributions will be either isotropically distributed for a background skymap, or distributed according to randomly generated sources following SFR for a signal skymap. The skymap is then used to evaluate the TS corresponding to the specific realization of the input parameters, and the TS value is saved. See Figure 5.1 for a simple flowchart of the signal and background approaches.

5.1.2 *General signal implementation approximations*

While there is no difference in approach for CRs and neutrinos in the background case, there are differences between the two in the signal case. Before we mention the specific complications for neutrinos and UHECRs and how they are dealt with, we will go through the main approximations and simplifications both species have in common. The following points denote the general implementation, and they hold true unless otherwise stated (e.g. in the case of the declination-dependent UHECR analysis):

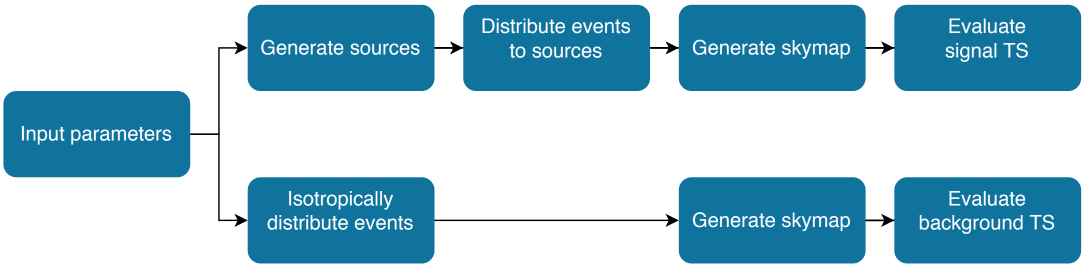

Figure 5.1: Flowchart of general implementation approach. First, a set of input parameters are read by the code, which are passed to the signal and background generation methods. The background method isotropically distributes N particles and creates a corresponding skymap. The signal method generates sources based on source density ρ_0. N particles are then distributed to the sources using Equation 4.3, and a skymap is generated using particle-specific input parameters. Both signal and background methods then evaluate the TS using the skymap.

- The sources do not follow large-scale structure, rather they are isotropically distributed in direction and distributed according to SFR in distance.
- The sources are only explicitly simulated within a sphere denoted by the radius corresponding to a redshift value z_{cut}. This mainly affects the neutrino analysis, and will be described below.
- The neutrinos and UHECRs do not follow an energy spectrum in effect, rather, they are thought of as above some threshold energy.
- The emission spectrum α, used in Equation 4.3, is set to $\alpha = 2$ for both particles.
- There is no declination or energy dependence on the effective area of our hypothetical detector.

Finally, the pixelization corresponds to an angular resolution of roughly $0.5°$, a value chosen due to its similarity to the angular resolutions of Auger and IceCube. No additional error on the angular resolution is added, meaning that undeflected particles will point straight back to their source.

5.1.3 *Neutrino implementation specifics*

The primary complications with the neutrino implementation relate to the fact that neutrinos come from faraway sources with no observable UHECR equivalents. These sources could come from sources at very high redshifts, so the immediate solution is to simulate up to very high redshifts. Unfortunately this does not function at high densities, as the number of sources rises to become computationally untenable. The solution chosen was to select a redshift z_{cut} after which sources are no longer explicitly simulated. One can estimate the fraction of observed particles stemming from sources within and outside the sphere denoted by z_{cut} through the two integrals $\xi_{in} = \int_0^{z_{cut}} \frac{\rho(z,\rho_0)}{H(z)} \mathrm{d}z$ and $\xi_{out} = \int_{z_{cut}}^{\infty} \frac{\rho(z,\rho_0)}{H(z)} \mathrm{d}z$ respectively. Assuming a total of N_ν signal neutrinos, the fraction of neutrinos not attributed to explicitly simulated sources is given by $N_{\nu,out} = N_{\nu}\frac{\xi_{out}}{\xi_{in}+\xi_{out}}$. These neutrinos are then isotropically distributed as a compromise. Naturally, the parameter z_{cut} must be selected so that it does not adversely affect the sensitivity estimation, but also in a fashion that minimizes the number of neutrino multiplets lost. All this must be balanced with the computational cost of increasing z_{cut}. For all extents and purposes of this thesis, it was found that $z_{cut} \approx 0.13$ both affected the sensitivity so negligibly as to have no impact, and was relatively computationally cheap.

The other main neutrino parameter is the signal-to-background ratio denoted S/B, which denotes an added fraction of isotropically distributed neutrino events on the skymap. This background corresponds to observed neutrinos above the energy threshold that are not related to sources of observable CR. In practice, this for instance be neutrinos stemming from UHECR sources at distances $D \gg D_{GZK}$, cosmogenic neutrinos, neutrinos stemming from UHECR $p + p$ interactions in molecular clouds that are not angularly correlated with the source direction or neutrinos created in the atmosphere from CR cascades.

5.1.4 *CR implementation specifics*

The primary characteristics of the UHECRs are their inevitable displacement due to magnetic deflection, and the flux suppression caused by the GZK effect. The implementations of both effects are subject to a number of simplifications. Firstly, the magnetic deflection experienced by the UHECRs from a source at a certain distance d_C is calculated using Equation 4.22, and as previously mentioned, all UHECRs are simulated with the same effective energy. Furthermore, a single set of EGMF parameters are used, leaving the expectation value for the deflection θ_s as a function of source distance only. Using θ_s, the angular displacement for individual CRs is generated randomly using a von Mises distribution with θ_s being the median value [48]. The new CR event position was calculated using the following rotation matrix

$$\begin{pmatrix} x \\ y \\ z \end{pmatrix} = \begin{pmatrix} \cos\varphi\cos\vartheta\sin\alpha\cos t - \sin\varphi\sin\alpha\sin t + \cos\varphi\sin\vartheta\cos\alpha \\ \sin\varphi\cos\vartheta\sin\alpha\cos t + \cos\varphi\sin\alpha\sin t + \sin\varphi\sin\vartheta\cos\alpha \\ -\sin\vartheta\sin\alpha\cos t + \cos\vartheta\cos\alpha \end{pmatrix} \tag{5.1}$$

Where $\begin{pmatrix} x \\ y \\ z \end{pmatrix}$ is the Cartesian coordinates of the magnetically deflected event on the surface of a sphere, (φ, ϑ) is the spherical coordinates of the CR source, α is the angular displacement from the source sampled from the von Mises distribution and $0 \leq t \leq 2\pi$ is the random rotation accompanying the angular displacement. A full derivation of the equation above can be found in Appendix A.2. An important note on the magnetic deflection implementation is that diffusion effects suffered by UHECRs from propagating in magnetic fields are ignored, and so too is the effect of time delay in observation caused by magnetic deflection.

The suppression caused by the GZK effect is implemented to result in both a reduction of flux from far-away source, along with a hard-cutoff past a certain distance in lieu of an actual energy spectrum for the UHECRs. The suppression is effectively an exponential attenuation, and rather than calculate interaction rates during particle propagation, the degree of suppression experienced by UHECRs stemming from a source at distance d_C is implemented as a factor $\exp\left(-\frac{d_C}{d_{GZK}}\right)$ in the calculation of the expected flux from a source. This does not take into account the increased distance traveled by UHECRs experiencing significant magnetic deflection. The value for d_{GZK} was evaluated using the simulations of the expected source flux as a function of CR energy from [49]. The hard cutoff sets the expectation flux for sources outside some critical redshift z_{GZK} to $\lambda_{CR}\,(z > z_{GZK}) = 0$. The value of z_{GZK} chosen corresponded to $d_{LTD} = 300$Mpc.

5.2 *Typical simulation results*

This section briefly visually introduces the notion of the 'skymap', along with examples from Monte Carlo simulation. As mentioned, each realization of a universe given some input parameters will result in a skymap, which is the binned (pixelized) distribution of events on the celestial sphere. These skymaps can be visually represented in 2D through Mollweide projection, which has proven to be an effective tool for both debugging and understanding data results. Examples of signal and background skymaps with $\rho = 10^{-6}\text{Mpc}^{-3}$, $N_\nu = N_{CR} = 2000$, $E = 60$EeV, $\theta_s = 3°$and $n_{side} = 2^6$ can be seen in Figures 5.2 and 5.3. Note that this example has low density, high numbers of observed particles and low magnetic deflection in order to make the qualitative differences between the maps pronounced. It is worth noting that in this example, one can see a large cluster of CR events in the western hemisphere, and a multiplet of 4 neutrinos is also present in the same location - an ideal scenario. Several seemingly uncorrelated multiplets are also present in the ν-map however. Furthermore, note the qualitative similarity between the signal and background ν-maps. This highlights the near-isotropic appearance of even non-isotropic ν-maps at low event numbers.

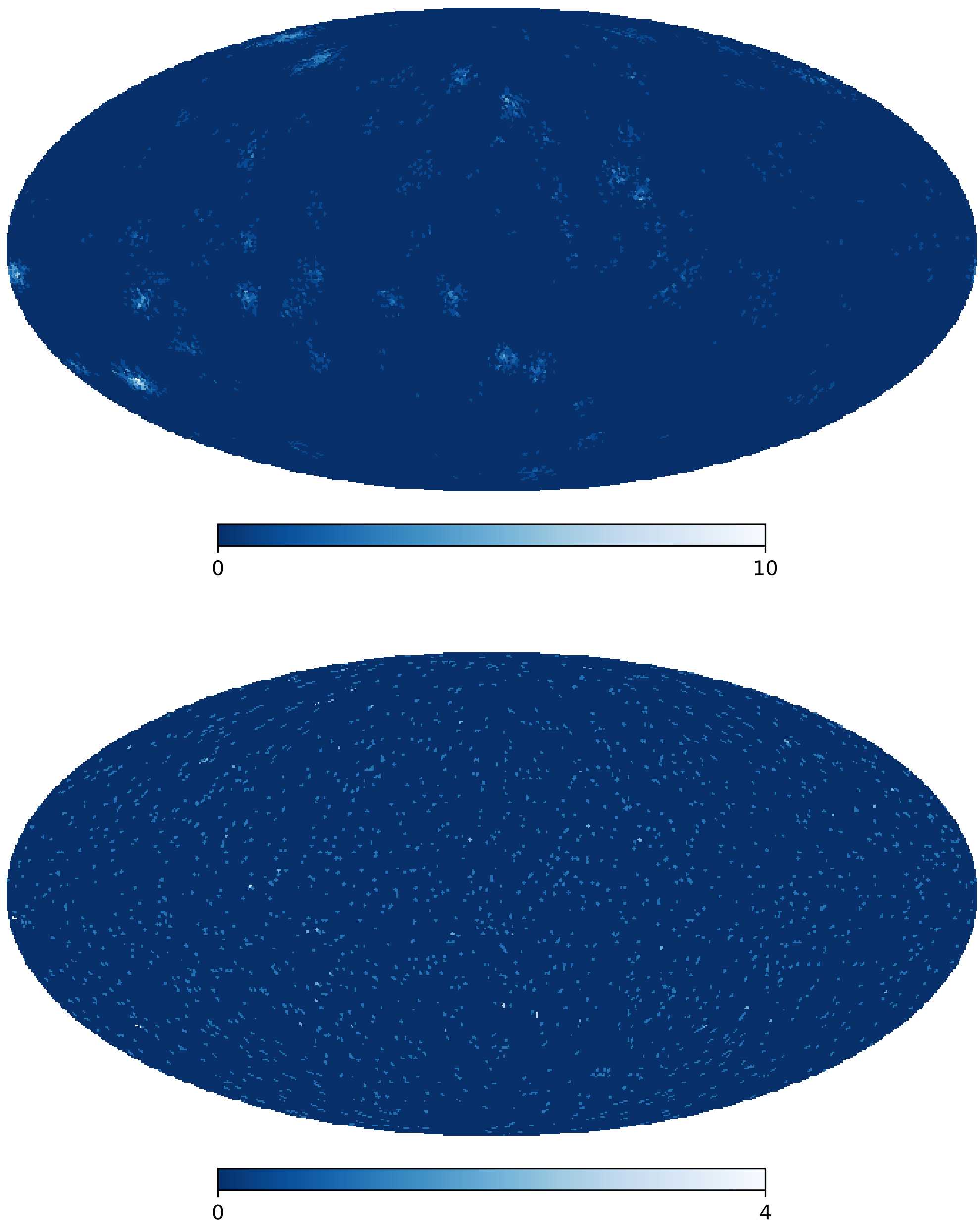

Figure 5.2: Top: Signal CR skymap consisting of magnetically deflected CR events stemming from explicitly simulated sources. Bottom: Signal ν skymap consisting of sources both correlated and uncorrelated with CR events. All sources within a given redshift $z_{cut} = 0.15$ emit both neutrinos and UHECRs.

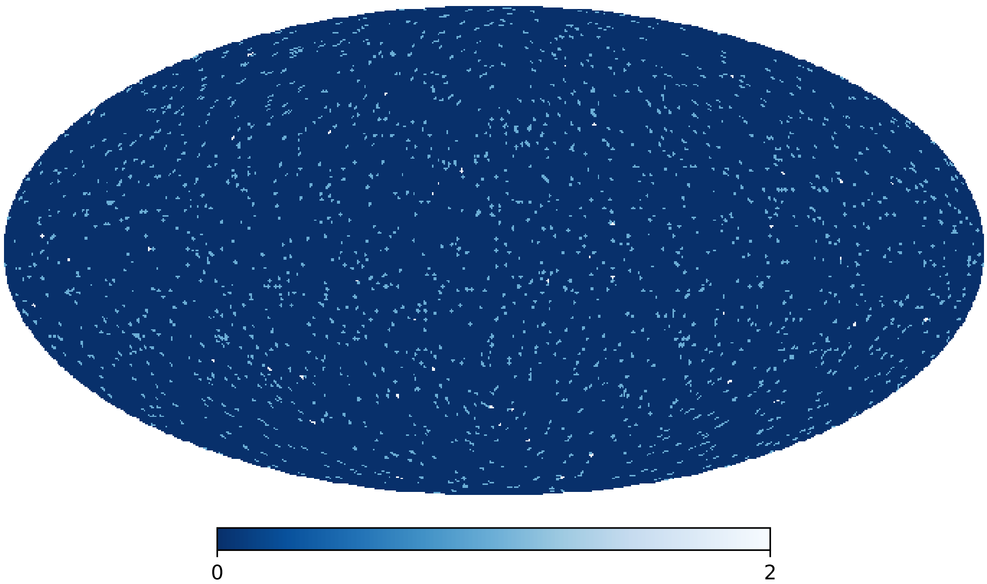

Figure 5.3: Background skymap with $N_{events} = 2000$ isotropically distributed events.

5.3 *Consistency checks*

There are two primary consistency checks to showcase for the simulation - namely that of correct source distribution, and that of flux distribution. By analytically evaluating the expectation distribution, it can be shown through simulations of multiple universes that the code produces the expected results.

5.3.1 *Redshift distribution of sources*

A simple way to evaluate the expected number of sources as a function of redshift is to discretize the problem and then evaluate this function. Using Equation 4.7, we evaluate the expected number of sources at 100 logarithmically spaced values of z between $z_{min} = 10^{-2}$ and $z_{max} = 6$. Then, the actual number of sources within the sphere denoted by these redshifts is evaluated in a simulated universe, and one obtains Figure 5.4. As can be seen in the figure, there are some minor statistical overfluctuations at low redshifts, but otherwise the shape of the distribution agrees excellently with the expectation.

5.4 *Distribution of source flux*

Evaluating the distribution of flux $\frac{dN_{source}}{d\lambda_{PS}}$ is the most effective single consistency check available, as it allows one to see if the entire flux normalization method functions as expected. Finding an analytical expression for the expected distribution is however more complicated than was the case for the radial source distribution. We will now derive an expression for $\frac{dN_{source}}{d\lambda_{PS}}$:

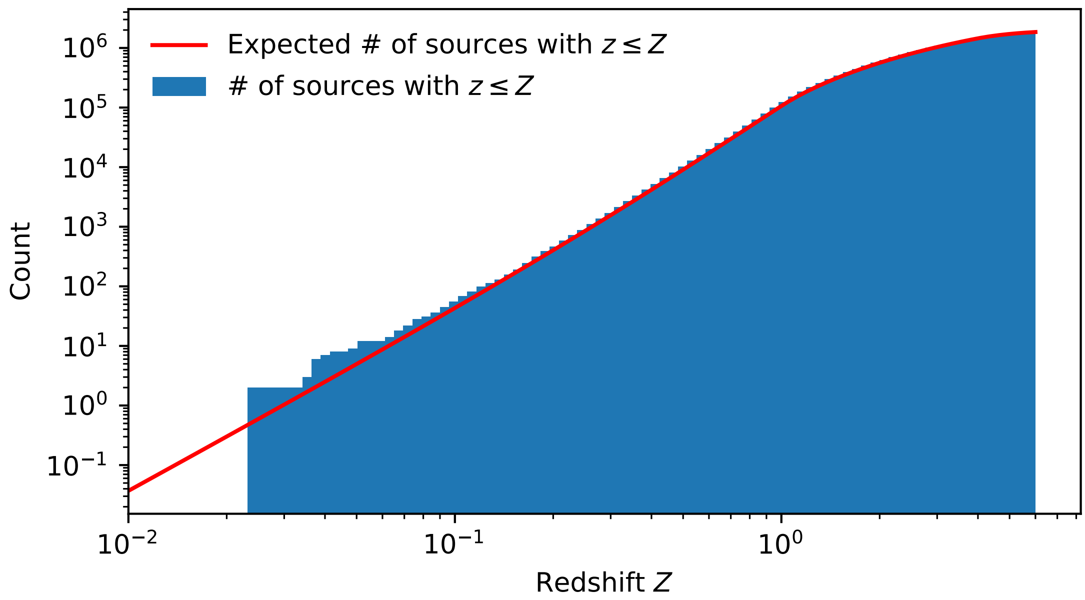

Figure 5.4: Cumulative distribution of number of sources as a function of redshift for an single realization compared to the expected number of sources. Evaluated using $\rho_0 = 10^{-7}\text{Mpc}^{-3}$. There are slight overfluctuations at low numbers of sources.

The strategy here is to evaluate $\frac{\mathrm{d}N_{source}}{\mathrm{d}z}$ and $\frac{\mathrm{d}\lambda_{PS}}{\mathrm{d}z}$, as we then have $\frac{\frac{\mathrm{d}N_{source}}{\mathrm{d}z}}{\frac{\mathrm{d}\lambda_{PS}}{\mathrm{d}z}} = \frac{\mathrm{d}N_{source}}{\mathrm{d}\lambda_{PS}}$. First we compute $\frac{\mathrm{d}N_{source}}{\mathrm{d}z}$ by differentiating Equation 4.7 wrt. z, yielding

$$\frac{\mathrm{d}N_{source}}{\mathrm{d}z} = \frac{c}{H(z)} 4\pi d_C^2 \rho(z) \tag{5.2}$$

Next, we compute $\frac{\mathrm{d}\lambda_{PS}}{\mathrm{d}z}$. We start from Equation 4.16, and use the substitution $K = A_{eff}(\Omega)\, T_{live} Q_0 \zeta$ to obtain:

$$\lambda_{PS}(z) = \frac{K}{4\pi d_L^2}(1+z)^{2-\alpha} = \frac{K}{4\pi d_C^2}(1+z)^{-\alpha} \tag{5.3}$$

This gives us

$$\frac{\mathrm{d}\lambda_{PS}}{\mathrm{d}z} = \frac{K}{4\pi}\left(\left(\frac{\mathrm{d}}{\mathrm{d}z}\frac{1}{d_C^2}\right)(1+z)^{-\alpha} + \left(\frac{\mathrm{d}}{\mathrm{d}z}(1+z)^{-\alpha}\right)\frac{1}{d_C^2}\right) \tag{5.4}$$

Where

$$\frac{\mathrm{d}}{\mathrm{d}z}\frac{1}{d_C^2} = -2\frac{1}{d_C^3}\frac{c}{H(z)} \tag{5.5}$$

and

$$\frac{\mathrm{d}}{\mathrm{d}z}(1+z)^{-\alpha} = -\alpha(1+z)^{-\alpha-1} \tag{5.6}$$

Leading to

$$\frac{\mathrm{d}\lambda_{PS}}{\mathrm{d}z} = \frac{K}{4\pi}\left(-2\frac{1}{d_C^3}\frac{c}{H(z)}(1+z)^{-\alpha} - \alpha(1+z)^{-\alpha-1}\frac{1}{d_C^2}\right) = -\frac{K}{4\pi}\frac{2cH(z)^{-1}+\alpha(1+z)^{-1}d_C}{(1+z)^{\alpha}d_C^3} \tag{5.7}$$

Thus, we obtain

$$\frac{\mathrm{d}N_{source}}{\mathrm{d}\lambda_{PS}} = \frac{\frac{\mathrm{d}N_{source}}{\mathrm{d}z}}{\frac{\mathrm{d}\lambda_{PS}}{\mathrm{d}z}} = -\frac{\frac{c}{H(z)}4\pi d_C^2\rho(z)}{\frac{K}{4\pi}\frac{2cH(z)^{-1}+\alpha(1+z)^{-1}d_C}{(1+z)^{\alpha}d_C^3}} = -\frac{4^2\pi^2 d_C^5(1+z)^{\alpha}\rho(z)c}{KH(z)\left(2cH(z)^{-1}+\alpha(1+z)^{-1}d_C\right)} \tag{5.8}$$

To obtain an expression for d_C, we use $\lambda_{PS} = F = \frac{K}{4\pi d_C^2}(1+z)^{-\alpha}$ and obtain $d_C = \sqrt{\frac{K}{4\pi F}(1+z)^{-\alpha}}$. In order to rewrite z, we interpolate to obtain $z(d_C)$, giving us $z(d_C(F))$, leading to

$$d_C(F) = \sqrt{\frac{K}{4\pi F}(1+z(d_C))^{-\alpha}} \tag{5.9}$$

Note that the expression for $d_C(F)$ is non-linear. This is solved by finding the root of the function $f(d) = d_C(F) - \sqrt{\frac{K}{4\pi F}(1+z(d_C))^{-\alpha}}$, which is achieved by using a numerical root-solver, such as *fsolve*. Now we remove the factor K by inserting our expression for Q_0 given by $Q_0 = \frac{N_\nu}{T_{live}A_{eff}}\frac{1}{c}\frac{1}{\xi\zeta}$ into $K = A_{eff}(\Omega)T_{live}Q_0\zeta$, which for Equations 5.8 and 5.9 gives us

$$\begin{aligned}
\frac{\mathrm{d}N_{source}}{\mathrm{d}\lambda_{PS}} &= -\frac{1}{A_{eff}(\Omega)T_{live}Q_0\zeta}\frac{4^2\pi^2 d_C^5(1+z)^{\alpha}\rho(z)c}{H(z)\left(2cH(z)^{-1}+\alpha(1+z)^{-1}d_C\right)} \\
&= -\frac{1}{\frac{N_\nu}{T_{live}A_{eff}}\frac{1}{c}\frac{1}{\xi\zeta}}\frac{1}{A_{eff}(\Omega)T_{live}\zeta}\frac{4^2\pi^2 d_C^5(1+z)^{\alpha}\rho(z)c}{H(z)\left(2cH(z)^{-1}+\alpha(1+z)^{-1}d_C\right)} \\
&= -\frac{c\xi}{N_\nu}\frac{4^2\pi^2 d_C^5(1+z)^{\alpha}\rho(z)c}{H(z)\left(2cH(z)^{-1}+\alpha(1+z)^{-1}d_C\right)}
\end{aligned} \tag{5.10}$$

And

$$d_C(F) = \sqrt{\frac{N_\nu}{T_{live}A_{eff}}\frac{1}{c}\frac{1}{\xi\zeta}\frac{A_{eff}(\Omega)T_{live}\zeta}{4\pi F}(1+z(d_C))^{-\alpha}} = \sqrt{\frac{N_\nu}{c\xi}\frac{1}{4\pi F}(1+z(d_C))^{-\alpha}} \tag{5.11}$$

Using this expression for $\frac{\mathrm{d}N_{source}}{\mathrm{d}\lambda_{PS}}$ we can then evaluate the distribution of expected observed flux from neutrino sources λ_ν. Furthermore, we can use this quantity to evaluate the singlet and multiplet expectations at the corresponding values of λ_ν through the equations $n_{singlet}(\lambda_\nu) = \frac{\mathrm{d}N_{source}}{\mathrm{d}\lambda_\nu}(1-\exp(-\lambda_\nu))$ and $n_{multiplet}(\lambda_\nu) = \frac{\mathrm{d}N_{source}}{\mathrm{d}\lambda_\nu}(1-\exp(-\lambda_\nu)(1+\lambda_\nu))$, where the two factors at the end are given by the Poisson probabilities for a single source to produce observed singlets and multiplets respectively. Using these expressions, we produce Figure 5.5, which shows an excellent agreement between the simulated data and theoretical prediction given

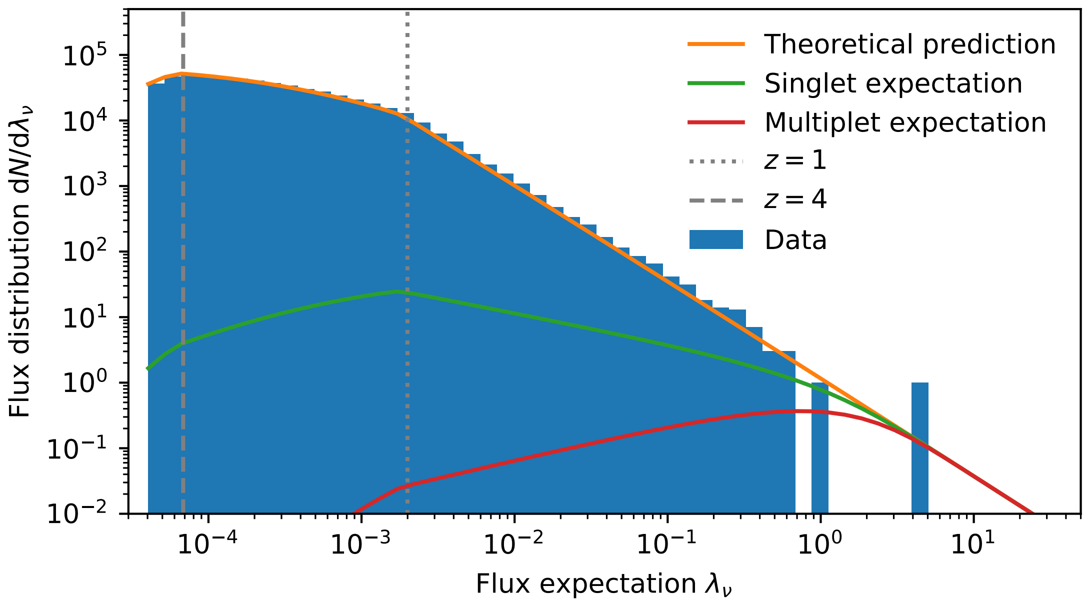

Figure 5.5: Distribution of expected observed flux from neutrino sources up to $z = 5$, with $\rho_0 = 3 \cdot 10^{-8}\text{Mpc}^{-3}$ and $N_\nu = 400$ given by the blue histogram. The orange solid line indicates the predicted distribution given by Equation 5.10. The green and red solid lines indicate the expected amount of singlets and multiplets at a given flux. The dotted and dashed lines indicate the flux values corresponding to sources at distances $z = 1$ & $z = 4$.

by Equation 5.10. Furthermore, it serves as an additional confirmation that SFR has been correctly implemented, as the features in the data clearly correspond to $z = 1$ and $z = 4$, which is the redshifts at which the features of SFR should affect the distribution. While the plot shown here is for neutrino emission, a similar plot could be produced following the same approach for CRs, the only difference being the addition of the exponential suppression from the GZK effect.

6 NEUTRINO ANALYSIS

In this chapter we will first describe the test statistic specific to the neutrino analysis. Then the results of the analysis will be presented and discussed.

6.1 *The all-sky point source test statistic*

To formally introduce the all-sky point source (PS) TS for neutrinos, we first express the two hypotheses. The signal hypothesis H_1: The data sample in question contains both signal neutrinos, i.e. neutrinos coming from a single source with a certain signal strength, and background neutrinos, meaning neutrinos that are either purely atmospheric, or are from a diffusive astrophysical background. The background hypothesis H_0: The data sample in question contains only background neutrinos. Given a sufficiently large sample of data, one would expect clusters of neutrinos in the direction of sources, should the signal hypothesis be true. If it were not, then the neutrinos should be isotropically distributed.

The TS is defined as

$$TS_{PS} = 2 \ln \left(\frac{\mathcal{L}\left(\text{Data}|H_1\right)}{\mathcal{L}\left(\text{Data}|H_0\right)} \right), \tag{6.1}$$

with $\mathcal{L}\left(\text{Data}|H_1\right)$ being the likelihood of the hypothesis H_1 given the data. Here the unbinned likelihood is used and evaluated in a single pixel using the expression [50]

$$\mathcal{L}\left(\text{Data}|H_1\right) = \mathcal{L}\left(n_s\right) = \prod_i^N \left(\frac{n_s}{N} S_i + \left(1 - \frac{n_s}{N}\right) B_i \right). \tag{6.2}$$

Where the product is over the N observed events, and n_s is the number of signal events in the pixel. S_i and B_i correspond to the signal and background probabilities of event i respectively. These are the signal and background hypotheses, and essentially designate a probability to the nature of the individual event. The signal hypothesis, as mentioned earlier, postulates the presence of point source(s), and as the background hypothesis postulates an isotropic distribution of observed events, S_i and B_i are implemented in a way which reflects that. The likelihood quantity is maximized for a non-negative n_s, leading to the most likely number of events in a pixel. Thus, the expression for the point source TS can also be written using $\mathcal{L}\left(n_s\right)$ as

$$TS_{PS} = -2 \ln \left(\frac{\mathcal{L}\left(n_{s,max}\right)}{\mathcal{L}\left(0\right)} \right). \tag{6.3}$$

For this reason, the method is also called the unbinned maximum likehood ratio test. As pointed out, this method only returns the TS value of a single pixel, but one can sequentially calculate the values for all pixels, which will result in a skymap of TS values. This approach is called an all-sky search, and is a common method used in the search for neutrino point sources. It allows for the analysis of neutrino clustering against the null hypothesis of no clustering. The choice of signal hypothesis used in this thesis is that of a 'Dirac delta function signal'. This means that for all events inside the respective pixel in which the likelihood is being evaluated, $S_i = 1$, and $S_i = 0$ for all other pixels. The reasoning behind this choice is threefold;

Firstly, this approach allows for an analytic expression (derived in Section 6.1.1) for the maximum likelihood, making this a computationally efficient method. Secondly, the arrival direction of a well-reconstructed neutrino would point directly back to its point of origin, and it is then assumed that no neutrino is falsely reconstructed as coming from another pixel than that of its source. Thirdly, more complicated multivariate signal hypotheses require careful analysis of the allowed parameter space in order to achieve realistic fits, rather than simply the best possible fit. Constraining the signal hypothesis to contain only one variable, the number of signal events n_s, the interpretation of results becomes markedly easier. Finally, the background hypothesis is given by $B_i = \frac{1}{N_{pix}}$, where N_{pix} is the total number of pixels.

As there is interest in a single TS value per sample, and it would be most likely that the pixel with the greatest amount of neutrino events (and thus also highest TS value) contains one or more sources, the final TS value evaluated per sample is that of the brightest pixel, referred to as the all-sky maximum likelihood (MLH) TS.

For the unbinned maximum likelihood ratio test, the behavior is well known. A distribution consisting solely of background events will return a χ^2 distribution, with the number of degrees of freedom (DoF) depending on the dimensionality of the TS. In the case of this analysis, the χ^2 has 1 DoF [51]. This allows one to forego calculating background distributions entirely. A greatly exaggerated example of a signal and background distribution in the full MLH case (that is, not just the maximum) can be seen in Figure 6.1, where a 1-DoF scaled χ^2 distribution has been included to show its direct relation to the background distribution. Unfortunately, it was deemed outside the scope of the project to investigate the nature of the maximum MLH TS distribution, and thus it was necessary to manually calculate the background distribution. An example of background distribution, along with two signal distributions from actual simulated data can be seen in Figure 6.2. The reason for the low amount of bins used in the figure is due to the nature of Dirac delta signal, which causes the number of possible TS values to become discrete, as the number of neutrinos in each pixel is discrete. If a high number of bins was chosen, the bins would have a clear seperation between them, and the overall trend would be less obvious.

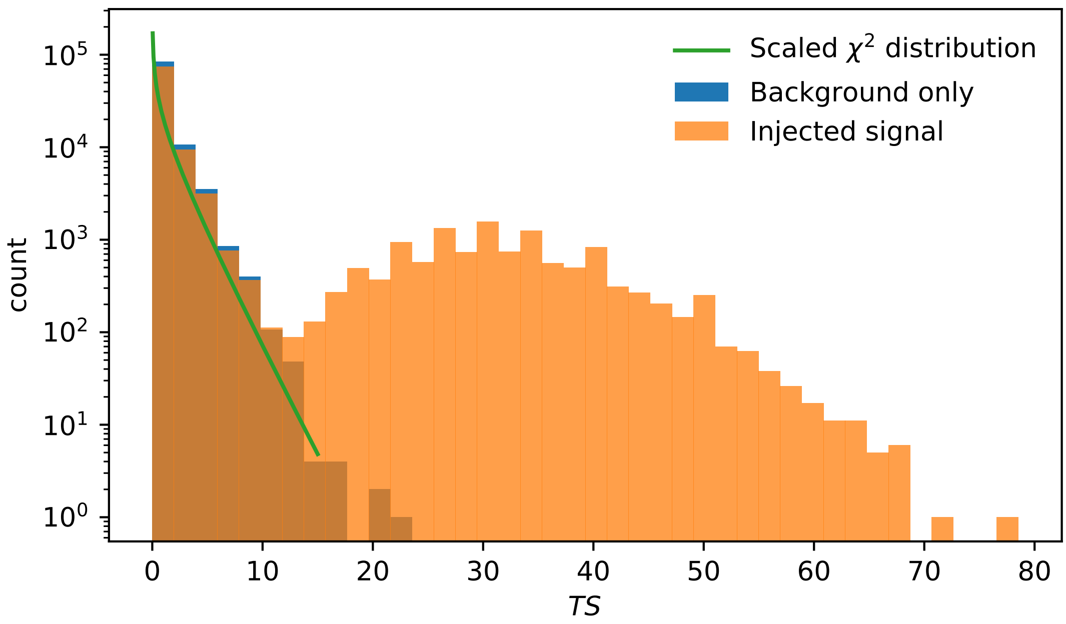

Figure 6.1: TS_{PS} distributions for mock data with background only and injected signal, along with a χ^2 distribution to showcase Wilk's theorem. Made with 10^5 pixels, each with a poisson-sampled amount of events from an expectation value of $\lambda = 40$, constituting an isotropic background. The signal case has a value of λ added to $1/4$ of the pixels, producing the tail-end which is clearly seperate from the background distribution.

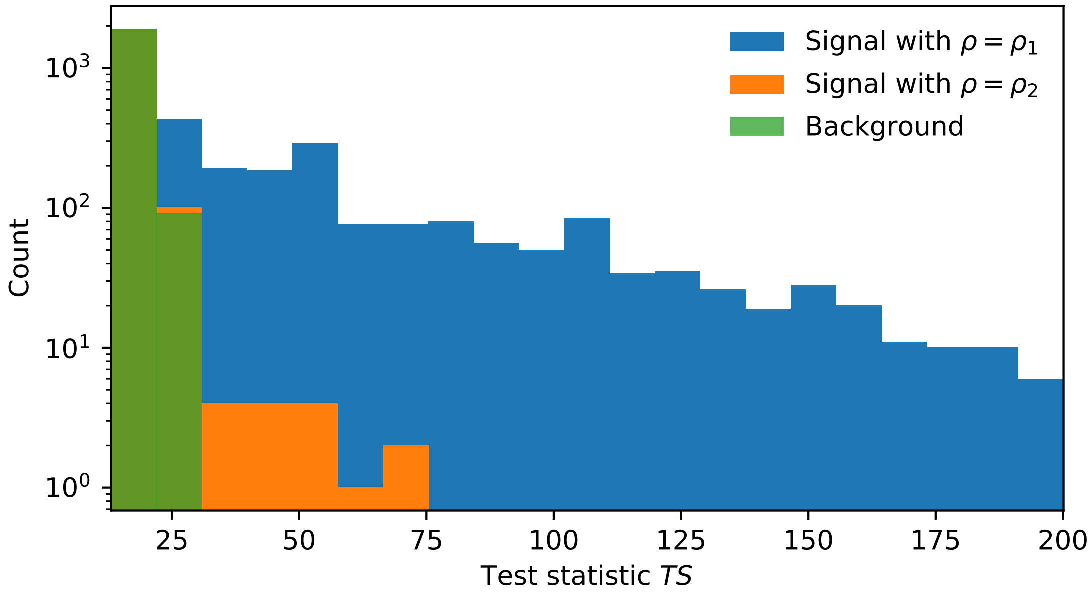

Figure 6.2: Example distributions for background and signal for the maximum MLH TS. Taken from simulation with $N_\nu \approx 1400$, $\rho_1 = 10^{-7}\text{Mpc}^{-3}$,$\rho_2 = 5 \cdot 10^{-4}\text{Mpc}^{-3}$ and $n_{samples} = 2000$. The highest-value bin corresponds to the 98th percentile of the signal distribution.

6.1.1 *Derivation of the TS_{PS} given the dirac delta function signal hypothesis*

We have that $\mathcal{L}(n_s) = \prod_{i=1}^{N}\left[\frac{n_s}{N}S_i + \left(1 - \frac{n_s}{N}\right)B_i\right]$, and that $TS = 2\log\left(\frac{\mathcal{L}(n_s>0)}{\mathcal{L}(0)}\right)$, and that $S_i = \begin{cases} 1 & \text{if inside} \\ 0 & \text{if outside} \end{cases}$. This can be written out as:

$$TS = 2\log\left(\frac{\prod_{i=1}^{N}\left[\frac{n_s}{N}S_i + \left(1 - \frac{n_s}{N}\right)B_i\right]}{\prod_{i=1}^{N}\left[B_i\right]}\right) = 2\log\left(\prod_{i=1}^{N}\frac{\frac{n_s}{N}S_i + \left(1 - \frac{n_s}{N}\right)B_i}{B_i}\right). \tag{6.4}$$

Rewriting the product we obtain:

$$TS = 2\sum_{i=1}^{N}\log\left(\frac{\frac{n_s}{N}S_i + \left(1 - \frac{n_s}{N}\right)B_i}{B_i}\right). \tag{6.5}$$

We can then write this expression into two terms, one for events inside the pixel being considered, written as N_{in}, and one for events outside, written as N_{out}, resulting in:

$$\begin{aligned} TS &= 2\left[\sum_{i=1}^{N_{in}}\log\left(\frac{\frac{n_s}{N}+\left(1-\frac{n_s}{N}\right)B}{B}\right) + \sum_{i=1}^{N_{out}}\log\left(\frac{\left(1-\frac{n_s}{N}\right)B}{B}\right)\right] \\ &= 2\left[\sum_{i=1}^{N_{in}}\log\left(\frac{\frac{n_s}{N}}{B} + \left(1-\frac{n_s}{N}\right)\right) + \sum_{i=1}^{N_{out}}\log\left(1-\frac{n_s}{N}\right)\right] \end{aligned}. \tag{6.6}$$

Where we assume B to be constant for all i. This then allows us to write out the sums to obtain:

$$TS = 2\left[N_{in}\log\left(\frac{n_s}{BN} + \left(1-\frac{n_s}{N}\right)\right) + N_{out}\log\left(1-\frac{n_s}{N}\right)\right]. \tag{6.7}$$

This equation is then optimized. First we differentiate the expression:

$$\frac{\mathrm{d}}{\mathrm{d}n_s}2\left[N_{in}\log\left(\frac{n_s}{BN} + \left(1-\frac{n_s}{N}\right)\right) + N_{out}\log\left(1-\frac{n_s}{N}\right)\right] = 2\left[N_{in}\frac{\left(\frac{1}{BN}-\frac{1}{N}\right)}{\frac{n_s}{BN}+1-\frac{n_s}{N}} - N_{out}\frac{1}{N\left(1-\frac{n_s}{N}\right)}\right]. \tag{6.8}$$

We then solve for $\frac{\mathrm{d}}{\mathrm{d}n_s}TS = 0$ to obtain the n_s value corresponding to the maximum likelihood. We remove the factor of 2, as it will not affect the value for n_s:

$$N_{in}\frac{\left(\frac{1}{BN}-\frac{1}{N}\right)}{\frac{n_s}{BN}+1-\frac{n_s}{N}} - N_{out}\frac{1}{N\left(1-\frac{n_s}{N}\right)} = 0 \iff n_s = N_{in} + N_{out}\frac{B}{(B-1)}. \tag{6.9}$$

6.2 *Results & discussion*

The primary approach chosen to produce sensitivity results for this and the other analyses was to define a parameter space of interest, based on the primary observable variable (number of signal neutrinos observed N_ν in the case of this analysis) and the primary source variable, the local source density ρ. This parameter space was then investigated by discretizing it in logarithmically spaced combinations of ρ and N_ν, with m different values for ρ and n different values for N_ν, giving a total of $m \cdot n$ combinations. For each combination $n_{samples} = 2000$ simulations made to create a distribution of TS_S values. A single distribution of TS_B values was created for each value of N_ν. Using these distributions, it was possible to evaluate if the 90% sensitivity level is reached in every point on the grid.

The choice of the parameter space to investigate hinges on estimations of the densities of populations of astrophysical objects (ranging from $10^{-7}\mathrm{Mpc}^{-3}$ for large rich galaxy clusters to $10^{-3} - 10^{-2}\mathrm{Mpc}^{-3}$ for ordinary galaxies, with AGN and the like in between [49]). In the end, the range $\rho = 10^{-7} - 10^{-3.3}\mathrm{Mpc}^{-3}$ was deemed interesting in the case of the neutrino analysis, with $m = 30$. The chosen N_ν region was selected in order to both present a realistic scenario with current technology, but also to present one which is arguably realistic with new telescopes within the near future. The final range selected was $N_\nu = 40 - 4 \cdot 10^5$ with $n = 14$.

This parameter space was scanned twice, once for the signal-to-background ratio of $S/B = 0.1$, corresponding to the current IceCube value for neutrinos with $E > 10\mathrm{TeV}$ [43], and another time for the ideal case with no background at all, denoted $S/B = \infty$. Using the points of transition from between being sensitive and insensitive, a line can be made, above which the 90% sensitivity level is reached, and below which it is not. The sensitivity results for the two scans in the shape of such lines can be seen in Figure 6.3, with error-bars corresponding to the uncertainty imposed by the size of the logarithmic spacing. As can be seen, sensitivity is not reached before N_ν reaches the order of $\sim 10^3$ for both S/B cases. For comparison, IceCube's astrophysical neutrino data set used in [52] has fewer than 100 neutrino events with energies $E > 60\,\mathrm{TeV}$. Of these events, only a fraction allow for accurate arrival direction reconstruction. Furthermore, this is only true for densities below $\rho = 10^{-6}\mathrm{Mpc}^{-3}$, which is below limits set on the population density of UHECRs. At higher, more realistic densities, it is seen that the number of signal neutrinos observed increases well past $N_\nu = 10^4$, and in the case where $S/B = 0.1$, the total number of neutrinos observed, including background high energy neutrinos, would be above $N_{\nu,tot} = 10^5$. At the current time, observing such high numbers of neutrinos is unrealistic, a result which is consistent with point source searches carried out by IceCube on their cumulative astrophysical neutrino flux [53, 54]. This alludes to the difficulty with resolving neutrino point sources due to the very high mean free paths of neutrinos; the probability of observing multiplets from a neutrino source at low N_ν is extremely low due to the majority of the observed neutrino data stemming from distant sources.

That being said however, with the next generation of neutrino telescopes, such as IceCube Gen2 and KM3NeT [14, 15], to look forward to in the relatively near future, acquiring very large samples of neutrinos to reach the point of sensitivity may soon become realistic. Add to that, that the S/B value should fall over time as techniques and technology improves, which Figure 6.3 suggests could lower the required number of observed signal neutrinos by up to around half an order of magnitude, and that (more abundant) lower-energy neutrinos might also assist in the search for neutrino point sources. Finally, improvement of the angular resolution of neutrino arrival directions will allow for better sensitivity as well, as this will effectively increase the contrast between an isotropic background and a hypothetical neutrino point source with observed multiplets.

With all this in mind, one should not be disheartened by the current non-detection of neutrino point sources, as there are good reasons to believe that the future of neutrino astronomy, and its capacity to give new insight into hitherto open topics of astroparticle physics, is bright. One might still be tempted, however, to investigate different avenues of analysis, with a natural choice being the correlation of high energy neutrino events together with UHECRs, in the hopes of identifying their common sources faster.

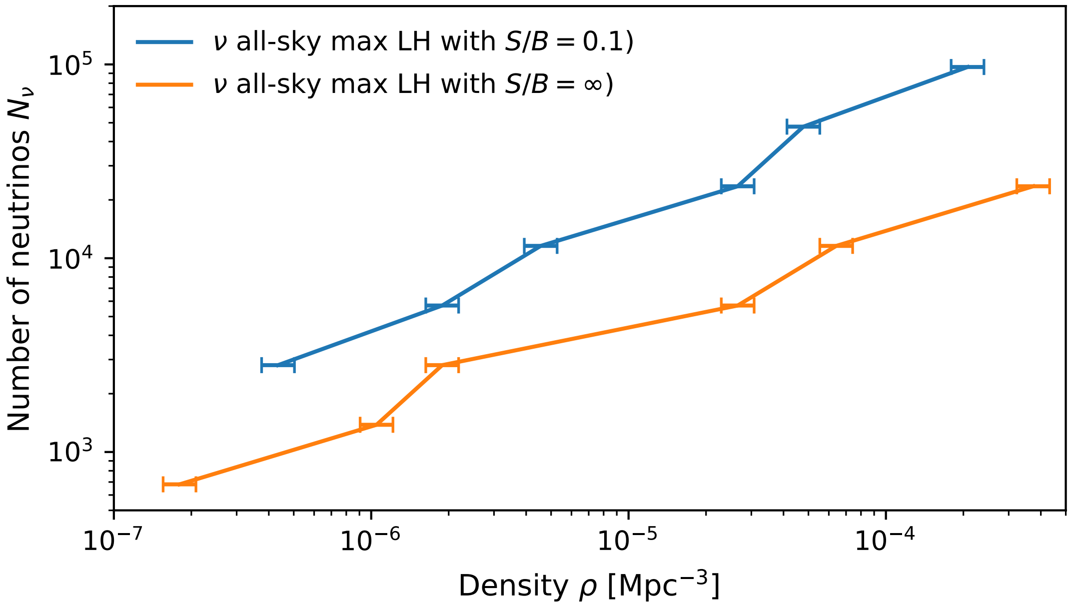

Figure 6.3: Results of neutrino sensitivity analyses using $S/B = 0.1$ and ∞. Source densities to the left of the lines are excluded by the 90% sensitivity limit.

7 COSMIC RAY ANALYSIS

Before joining together the neutrino and CR analyses into a single, joint analysis, we will first investigate the strength of an analysis purely using CRs. This section will first introduce the *TS* used for the CR analysis. Afterwards, it will present the results for CRs in two parts. The first part will present the results of the CR sensitivity analysis, exclusively based on Monte Carlo simulation. The second part will present the results of using public data from the PAO and TA.

7.1 *The Kolmogorov-Smirnov test statistic*

The definition of the Kolmogorov-Smirnov (KS) *TS* is motivated by the magnetic deflection of CRs: due to the fact that any UHECR will experience some level of deflection during propagation on its way to the Earth, its source, given a sufficient amount of observed UHECRs, will appear extended in the sky, with some characteristic angle extending from the true source, which should encompass the bulk of the CRs emitted by it. In reality, this effect could be further complicated e.g. by the introduction of correlated magnetic fields, but as mentioned before, these are not considered in this thesis. In any case, the PS TS, with it's Dirac delta signal hypothesis, was deemed unfit for the CR analysis. As mentioned in the section on the PS *TS*, one can use a signal hypothesis that allows for extended sources. This, however, is quite computationally expensive, and instead a new signal hypothesis is introduced for CRs. Rather than test for the presence of point sources, the signal hypothesis for the KS test tests for the presence of anisotropies. In order to do so, we introduce the cumulative two-point autocorrelation function given by

$$C\left(\{\boldsymbol{n}_i\}, \varphi\right) = \frac{2}{N\left(N-1\right)} \sum_{i=1}^{N} \sum_{j=1}^{i-1} \Theta\left(\cos\varphi_{ij} - \cos\varphi\right), \tag{7.1}$$

where N is the total number of events, $\{\boldsymbol{n}_i\}$ is a set of unit vectors pointing toward the observed arrival direction of the events, $\Theta\left(x\right)$ is the Heaviside step function and $\cos\varphi_{ij} = \boldsymbol{n}_i \cdot \boldsymbol{n}_j$ is the angular distance between two events. This function, at a given angle φ, calculates the number of pairs of events seperated at most by an angular distance of φ, with φ being confined to the interval $\varphi = [0, \pi]$. It is clear, however, that running the double sums is particularly computationally expensive, and thus an alternative approach is quite attractive.

The solution to this problem comes through spherical harmonics, specifically through what is known as the angular power spectrum. In the limit of large N, it becomes possible to approximate the distribution of events as a smooth function. As every smooth function on the surface of a sphere can be decomposed using spherical harmonics, it is also possible to decompose a skymap of events using spherical harmonics. This can be expressed as such:

$$g\left(\theta, \phi\right) = \sum_{l=0}^{\infty} \sum_{m=-l} a_{lm} Y_{lm}\left(\theta, \phi\right), \tag{7.2}$$

with l denoting the type of harmonic (e.g. $l = 0$ is a monopole, $l = 3$ is an octupole), m denoting which of the $2l+1$ independent solutions for a given l is specified, a_{lm} being a coefficient determining the contribution of Y_{lm} to the decomposition, and finally Y_{lm} being the spherical harmonic (e.g. $Y_{10} = \frac{1}{2}\sqrt{\frac{3}{\pi}}\cos\theta$). The angular power spectrum is defined by averaging the squares of all the a_{lm} coefficients for a given l, giving the expression

$$C_l = \frac{1}{2l+1} \sum_{m=-l}^{l} \left|a_{lm}\right|^2. \tag{7.3}$$

The angular power spectrum C_l thus gives insight in the contribution of each spherical harmonic to a decomposed function. However, its usefulness in this particular case comes from the relation between C_l and the differential two-point autocorrelation function $\zeta\left(\varphi\right)$ given by

$$\zeta\left(\varphi\right) = 2\pi \sum_{l} \left(2l+1\right) C_l P_l\left(\cos\varphi\right), \tag{7.4}$$

where $P_l\left(x\right)$ is the lth Legendre polynomial. Using this relation, we thus have a bridge from the power spectrum to the cumulative two-point autocorrelation function through $C\left(\varphi\right) = \int_{\cos\varphi}^{1} \zeta\left(\varphi'\right) \mathrm{d}\cos\varphi'$. The numerical implementation of this method relies on heavily optimized NumPy and SciPy packages, and is several orders of magnitude faster than using the double sum introduced earlier when $N \gtrsim 10^3$. Using the cumulative two-point autocorrelation function, the KS TS is then evaluated as follows: an isotropic distribution of events will, in the limit of $N \to \infty$, tend to $C\left(\varphi\right) = C_{iso}\left(\varphi\right) = 1/2\left(1 - \cos\varphi\right)$. The KS TS is then defined at the greatest difference between the background distribution $C_{iso}(\varphi)$ and the signal distribution $C(\varphi)$, formally expressed as

$$TS_{KS} = \sup_{\varphi} |C(\varphi) - C_{iso}(\varphi)| \tag{7.5}$$

for a given set of arrival directions $\{\boldsymbol{n}_i\}$. An increase in anisotropy will, in turn, lead to an increase in the corresponding TS_{KS} value. An example of a anisotropic $C(\varphi)$ compared to the isotropic $C_{iso}(\varphi)$ can be seen in Figures 7.1 and 7.2, with the corresponding TS_{KS} value in the legend.

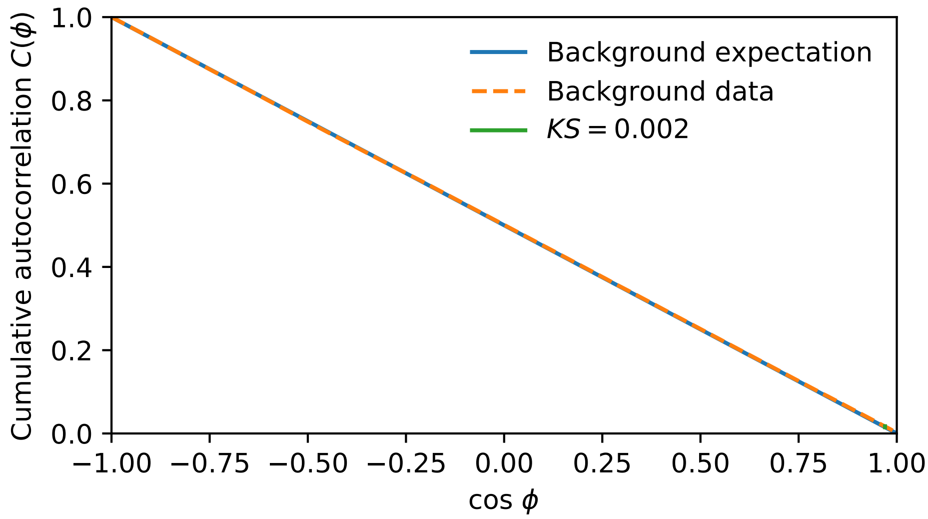

Figure 7.1: Example of a background KS value being evaluated for $N_{CR} = 500$ using Equation 7.4.

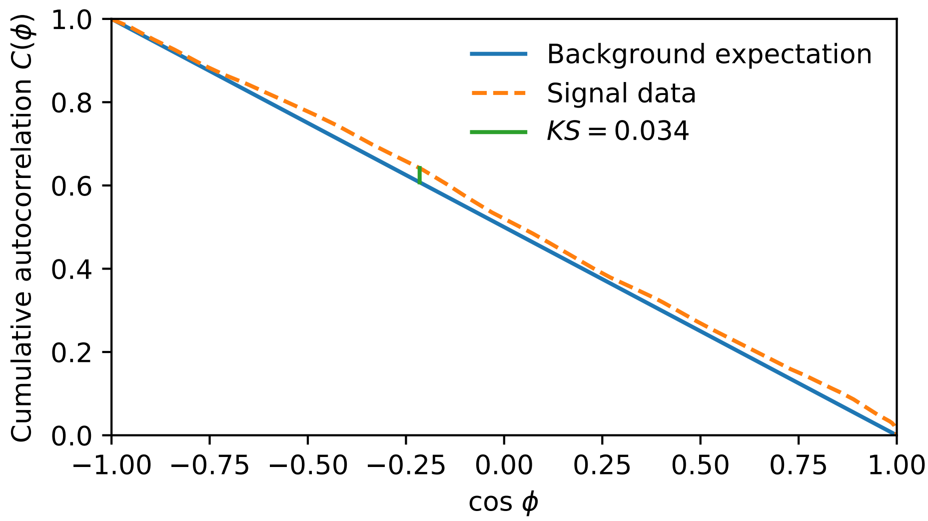

Figure 7.2: Example of a signal KS value being evaluated for $N_{CR} = 500$, $\rho_0 = 10^{-6}\text{Mpc}^{-3}$ and $\theta_s = 3°$ using Equation 7.4.

7.2 *An interlude on the cumulative two-point autocorrelation function*

During implementation of the Legendre polynomial-based cumulative two-point autocorrelation function, a deviation from the ideal background distribution C_{iso} was found in the case of low N_{CR}. The deviation would seemingly scale with $\cos\varphi$, and the magnitude of the offset would increase as $N_{CR} \to 0$ (see Figure 7.3 for an example of the phenomenon). To analyze the issue, comparisons were made between the KS evaluation methods based on Equations 7.1 and 7.4 - from now on the 'paircounting method' and 'Legendre method' respectively. Since the paircounting method should be slower in situations where N_{CR} is high, but adequately fast in $N_{CR} \to 0$ scenarios, it served well as a consistency check, seeing as the results produced by the method were known to be correct. It was found that the offset at its maximum at $\cos\varphi = 1$ scaled directly with $1/N_{CR}$. This was related to the fact that the method doublecounted each CR event once, which will be shown to be the case below. Using the following approach, a general solution to the offset issue is found: we start from some normalized event distribution of CRs g which is a function of position on the surface of a sphere Ω, given by

$$g(\Omega) = \frac{1}{N_{CR}} \sum_{i=1}^{N_{CR}} \delta\left(\hat{\boldsymbol{n}}(\Omega) - \hat{\boldsymbol{n}}_i\right), \tag{7.6}$$

where $\delta(x-a)$ is a delta function, $\hat{\boldsymbol{n}}(\Omega)$ denotes the unit vector of location Ω, and $\hat{\boldsymbol{n}}_i$ denotes the unit vector point to the location of CR event i. We then have the smooth cumulative two-point autocorrelation function given by

$$\widetilde{C}(\varphi) = \int d\Omega_1 \int d\Omega_2 g(\Omega_1)\, g(\Omega_2) \int_{\cos\varphi}^{1} d\cos\varphi'\, \delta\left(\hat{\boldsymbol{n}}(\Omega_1)\,\hat{\boldsymbol{n}}(\Omega_2) - \cos\varphi'\right), \tag{7.7}$$

where $\widetilde{C}$ is used instead of the C of Equation 7.1 because this method doublecounts - i.e. it counts each event as a pair with itself when $\cos\varphi = 1$. This expression can be rewritten by inserting Equation 7.6 into 7.7 and integrating the delta functions to obtain

$$\widetilde{C}(\varphi) = \frac{1}{N_{CR}^2} \sum_{i=1}^{N_{CR}} \sum_{j=1}^{N_{CR}} \Theta\left(\hat{\boldsymbol{n}}_i \hat{\boldsymbol{n}}_j - \cos\varphi\right),$$

where $\Theta(x-a)$ is the Heaviside step function. The sum can be rewritten to become

$$\widetilde{C}(\varphi) = \frac{1}{N_{CR}^2} \left(2 \sum_{i<j}^{N_{CR}} \Theta\left(\hat{\boldsymbol{n}}_i \hat{\boldsymbol{n}}_j - \cos\varphi\right) + \sum_{i=j}^{N_{CR}} \Theta\left(\hat{\boldsymbol{n}}_i \hat{\boldsymbol{n}}_j - \cos\varphi\right) \right), \tag{7.8}$$

where the first term can be thought of as the sum of the upper and lower triangular matrices above/below the diagonal in the $\hat{\boldsymbol{n}}_i \hat{\boldsymbol{n}}_j$ matrix of dimensions (i, j), and the second term being the trace. Using Equation 7.1 and that the trace term is $\sum_{i=j}^{N_{CR}} \Theta\left(\hat{\boldsymbol{n}}_i \hat{\boldsymbol{n}}_j - \cos\varphi\right) = N_{CR}$ we obtain

$$\widetilde{C}(\varphi) = \frac{N_{CR} - 1}{N_{CR}} C(\varphi) + \frac{1}{N_{CR}}. \tag{7.9}$$

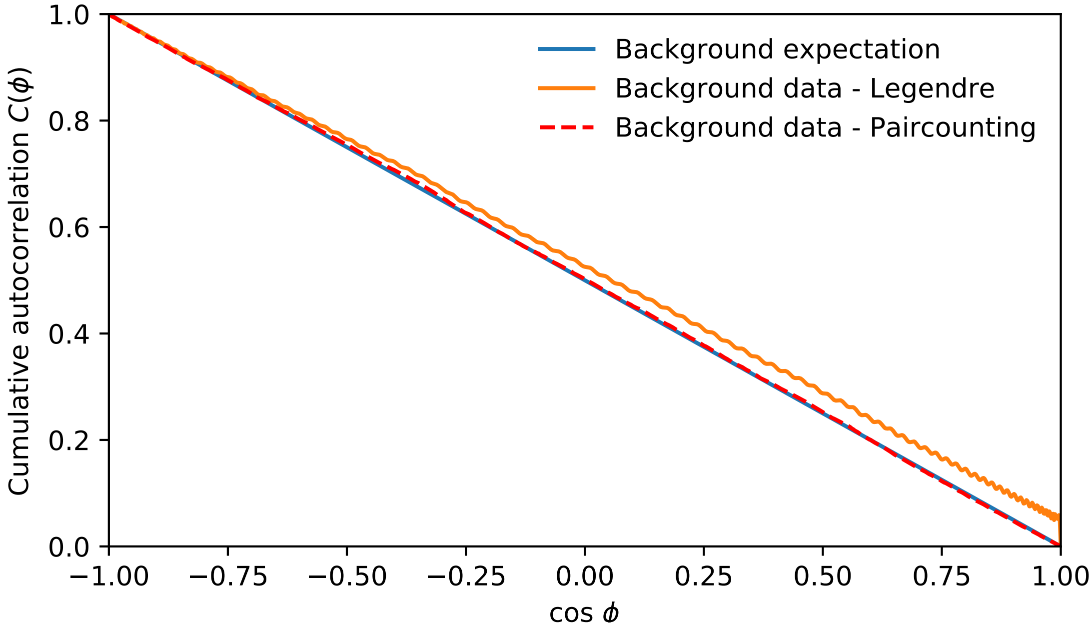

Figure 7.3: Resulting averaged cumulative two-point autocorrelation functions for the same background data, calculated using the two different methods. A clear offset at $\cos\varphi = 1$ is seen. Note that the sinusoidal behavior of the Legendre method was found to be universal (seen for both background and signal), and thus should have no impact on average.

A simple interpretation of the equation above is that if $C(\varphi)$ is the background expectation for the case $N_{CR} \to \infty$, then the background expectation for $N_{CR} \nrightarrow \infty$ is given by Equation 7.9. For an isotropically distributed background map with $C_{iso}(\varphi) = \frac{1}{2}(1 - \cos\varphi)$, this becomes:

$$\widetilde{C}_{iso}(\varphi) = \frac{N_{CR} - 1}{N_{CR}} \frac{1}{2}(1 - \cos\varphi) + \frac{1}{N_{CR}} = \frac{1}{2}(1 - \cos\varphi) + \frac{1}{N_{CR}} \frac{1}{2}(\cos\varphi + 1) . \tag{7.10}$$

Using this expression for $\widetilde{C}_{iso}(\varphi)$, we find an excellent fit for the expected background distribution, see Figure 7.4. It was confirmed through testing that the sensitivity using this modified Legendre method was identical to that of the paircounting method. An example of a background distribution, along with two signal distributions from actual simulated data can be seen in Figure 7.5.

7.3 *Results and discussion*

The CR analysis is divided into two parts, one general sensitivity analysis which consists entirely of simulated data, and one wherein the public UHECR data from Auger and TA is used to derive lower limits on the density of source ρ.

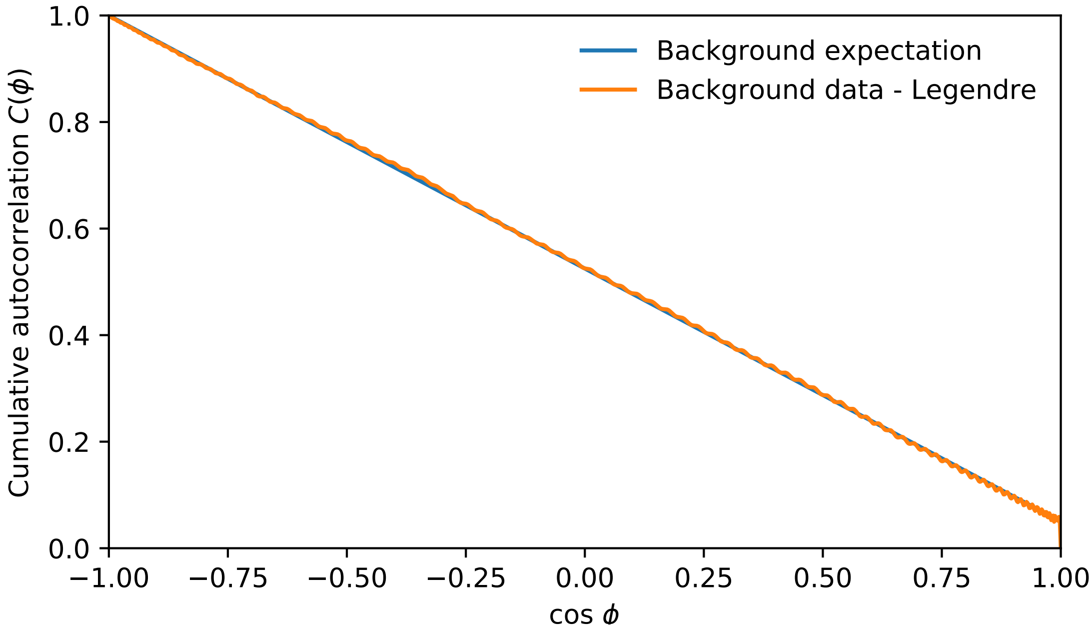

Figure 7.4: Resulting averaged cumulative two-point autocorrelation functions for the same background data with the Legendre method and the modified C_{iso} expression.

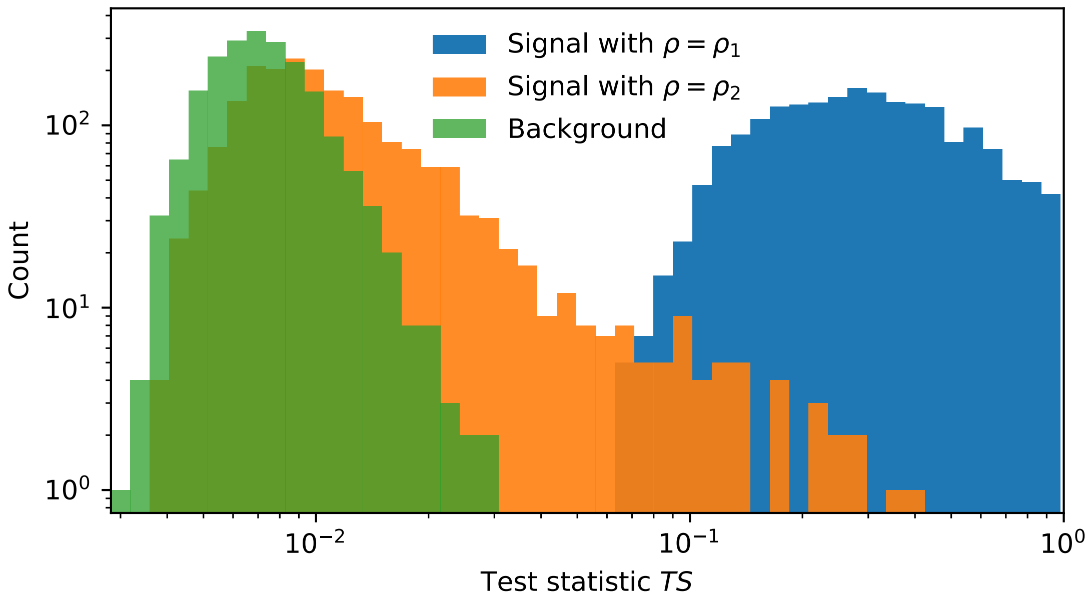

Figure 7.5: Example distributions for background and signal for the autocorrelation KS TS. Taken from simulation with $N_{CR} = 150$, $\rho_1 = 10^{-7}\text{Mpc}^{-3}$,$\rho_2 = 5 \cdot 10^{-4}\text{Mpc}^{-3}$ and $n_{samples} = 2000$. The top bin corresponds to the 99th percentile of the signal distribution.

7.3.1 *Sensitivity analysis*

The CR sensitivity analysis can be divided into two broad categories based on the characteristic scattering scale used, while all other input parameters remained constant, with $E_{CR} = 60\text{EeV}$, $Z = 1$, $d_{GZK} = 95\text{Mpc}$ and $z_{GZK} = 7.14 \cdot 10^{-2}$ (corresponding to 300Mpc). In both categories the expected deflection from the rGMF was fixed at $\theta_{s,rGMF} = 2.59°$, while the EGMF's contribution to the total deflection was either negligible or dominant. In the negligible EGMF case, the magnetic field parameters B and λ were parametrized according to Equation 4.22 with $\theta_s\,(D = 300\text{Mpc}) \approx 0.4°$, meaning that a 60EeV proton stemming from a source at a distance of 300Mpc would experience a displacement of 0.4° from the EGMF. In the dominant case, $\theta_s\,(D = 300\text{Mpc}) \approx 27.4°$. We note that the required values of B and λ for these parametrizations are within the allowed region mentioned in Section 4.4.3. The justification for these two scales at $\sim 3°$ and $\sim 30°$ is both the uncertainty on the true parameters of the EGMF, along with the uncertainty of the UHECR composition - should UHECRs primarily consist of heavier nuclei, the 30° scale would be closer to the real deflection scale experienced by UHECRs. It is important to underline that this is only partially true, as the deflection by the rGMF is unaffected by the choice of EGMF deflection scale.

Using the abovementioned input parameters, two scans were made over the density interval $\rho = 10^{-7} - 10^{-2.7}\text{Mpc}^{-3}$ and the number of CRs detected interval $N_{CR} = 10 - 1000$. The resulting sensitivity for the two deflection scenarios can be seen in Figure 7.6. In the plot, the lower limits on density set by Auger for similar deflection scales with $N_{CR} = 83$ are also included for comparison, with $\rho_{Auger}\,(\theta_s = 3°) = 4.5 \cdot 10^{-4}\text{Mpc}^{-3}$ and $\rho_{Auger}\,(\theta_s = 30°) = 2.5 \cdot 10^{-6}\text{Mpc}^{-3}$ [49]. Interestingly, it can be seen that there is a relatively small seperation between the two sensitivity lines in spite of the allowed deflection scale, while the seperation between the Auger results spans about two orders of magnitude. Furthermore, sensitivity is reached for $N_{CR} = 83$ with $\theta_s = 3°$ for this analysis at $\rho \approx 5 \cdot 10^{-5}\text{Mpc}^{-3}$, while it is reached for $\theta_s = 30°$ at $\rho \approx 2 \cdot 10^{-5}\text{Mpc}^{-3}$. The reason for the large disconnect between the Auger limits and our sensitivities could be attributed to the fact that the Auger analysis uses fixed deflection scales and declination dependence. The former means that e.g. at the $\theta_s = 30°$ scale, all CRs are effectively deflected by exactly 30° in the Auger analysis, while the implementation of the deflection in this analysis scales with distance, and allows for sampling of deflections both above and below the deflection at the distance D, $\theta_s\,(D)$. This means that very closeby sources will experience relatively little deflection in our implementation, resulting in greater anisotropies for the brightest sources.

The effect this has on the sensitivies of our analysis depends on the deflection scale. In the $\theta_s = 3°$ case, the dominant contributor to the deflection is the rGMF, meaning that the reduction of deflection experienced by UHECRs from nearby sources is of little import. The variability of the deflection caused by the von Mises sampling, however, will have the impact of causing roughly 1/2 of UHECR events to have deflections greater than 3°, thus reducing the sensitivity in this scenario. In the $\theta_s = 30°$ scenario, the EGMF is dominant, causing the reduction in angular displacement of UHECRs from nearby sources to improve sensitivity.

In addition to this, the aforementioned declination dependence restricts the observed CR events to a declination band, thus amplifying sources within the declination band for a fixed number of observed CRs, N_{CR}. Thus, these two effects could at least in part account for the disconnect observed.

There are other effects from the implementation choices that also affect the sensitivies found. For instance, the GZK effect implementation is not taking into account the additional distance traveled due to deflections. Thus, CRs coming from distant sources will be more abundant than is actually realistic, resulting in amplification of the observed flux from distant sources, which in turn decreases the overall sensitivity. This effect is mainly relevant in the 30° scale scenario, as the rGMF is the dominant source of deflection in the 3° scenario. This particular effect, however, is also present in the Auger analysis, and has no relation to the disparity seen between the Auger limits and our sensitivities.

These various implementation effects and differences motivate an analysis using declination dependence in conjunction with UHECR observational data from PAO and TA. This should have the effect of emphasizing the impact of the implementation differences, such as the deflection implementation difference, that are thought to be more realistic in the case of our implementation.

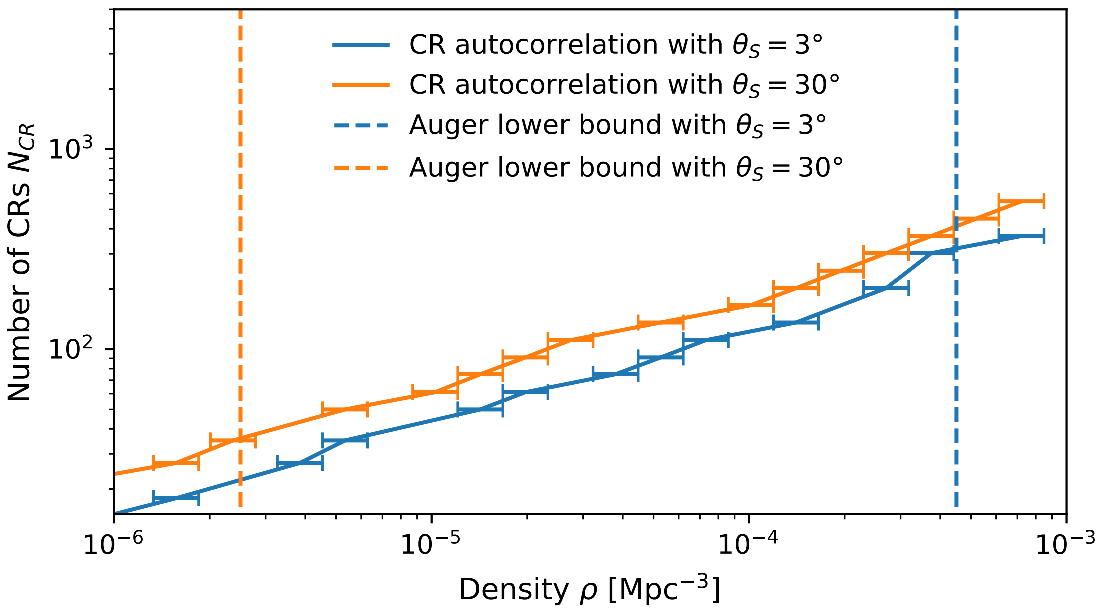

Figure 7.6: UHECR sensitivity lines, the solid lines correspond to the sensitivity analyses made in this thesis with the region to the left of the lines being excluded. The dashed lines correspond to lower limits set by Auger at the corresponding deflection scales with $N_{CR} = 83$ and $E_{CR} = 60$EeV. The error-bars correspond to the uncertainty imposed by the logarithmic spacing of ρ values.

7.3.2 *UHECR data analysis*

The public UHECR data from Auger and TA consists of 231 and 50 UHECR events respectively [5]. In order to match the TA data with the Auger data, the energies of the TA events was rescaled by $1/1.27$. Data selection was carried out using two energy thresholds, one with $E_1 > 50\text{EeV}$, and one with $E_2 > 60\text{EeV}$. The E_1 cut has $N_{Auger} = 231$ Auger events and $N_{TA} = 36$ TA events while the E_2 cut has $N_{Auger} = 132$ and $N_{TA} = 17$. The skymap resulting from the E_1 cut can be seen in Figure 7.7.

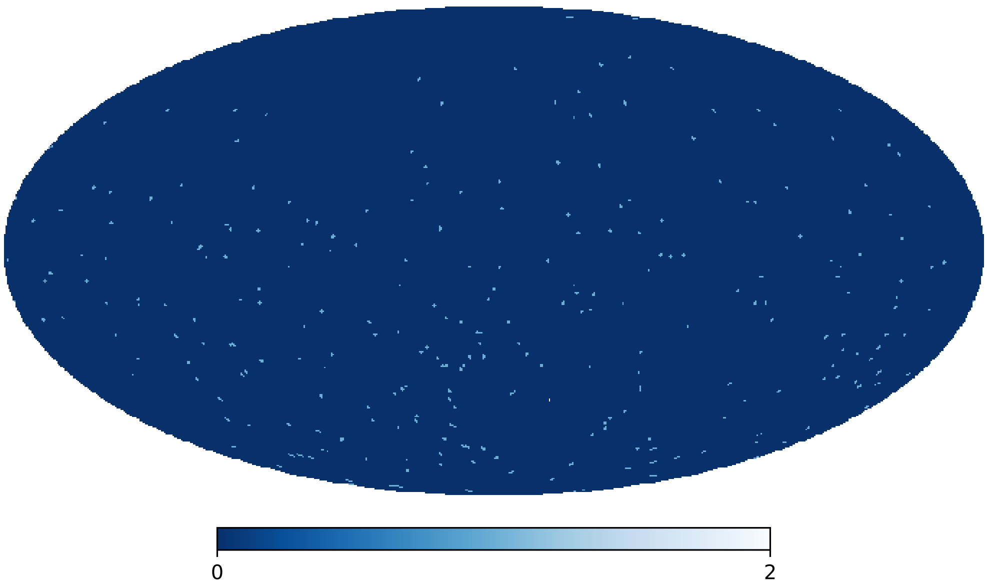

Figure 7.7: Skymap of the UHECR data with the E_1 cut.

Due to the declination dependence of exposure that the two observatories have, the signal and background data also had to be simulated using declination dependence. This was implemented under the assumption that both telescopes operated at full efficiency for any particle with a zenith angle $\theta < \theta_m$. The effect was modelled using weights on individual pixels in the skymap, depending on the declination δ of each pixel through the expression [55]

$$\omega(\delta) = \cos(a_0)\cos(\delta)\sin(\alpha_m) + a_m \sin(a_0)\sin(\delta) \tag{7.11}$$

where a_0 is the mean latitude of the detector and α_m is given by

$$\alpha_m = \begin{cases} 0 & \text{if } \xi > 1 \\ \pi & \text{if } \xi < -1 \\ \cos^{-1}(\xi) & \text{otherwise} \end{cases} \tag{7.12}$$

with

$$\xi \equiv \frac{\cos(\theta_m) - \sin(a_0)\sin(\delta)}{\cos(a_0)\cos(\delta)} \tag{7.13}$$

$\omega(\delta)$ is then calculated and normalized for both observatories, and the full declination dependence is calculated using

$$\omega_{full}(\delta) = \frac{\omega_{Auger}(\delta) N_{Auger} + \omega_{TA}(\delta) N_{TA}}{N_{Auger} + N_{TA}} \tag{7.14}$$

The corresponding values for Auger and TA were $a_{0,Auger} = -35.2°$ $\theta_{m,Auger} = 60°$ and $a_{0,TA} = +39.3°$, $\theta_{m,TA} = 55°$ respectively [5]. The resulting expected background map for the E_1 cut can be seen in Figure 7.8.

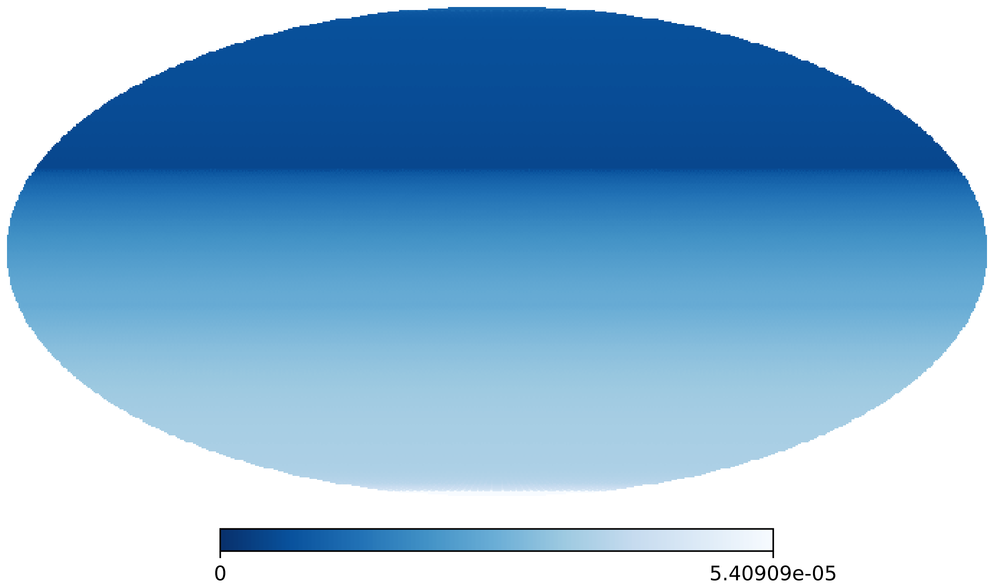

Figure 7.8: Map of normalized $\omega_{full}(\delta)$ values for each pixel using the E_1 cut. Note the increased exposure at both poles due to the maximum zenith angles of the observatories causing overlap.

In order to calculate the expected background two-point autocorrelation function, Equation 7.10 was utilized in conjunction with the Legendre method utilized on the ω_{full} skymap. during simulation. The TS values for the E_1 and E_2 skymaps were then found to be equal to $TS_1 = 2.08 \cdot 10^{-2}$ and $TS_2 = 1.72 \cdot 10^{-2}$ respectively. These TS values were compared to two distributions of background TS_B values made using the corresponding number of UHECRs, resulting in two statistically insignificant p-values of $p_1 = 17.30\%$ and $p_2 = 48.95\%$. The lower limits set on the density were then found by identifying the densities at which 90% of the TS_S distribution is equal to or greater than TS_1 and TS_2. This was done for both the $\theta_1 = 3°$ and $\theta_2 = 30°$ scale deflection scenarios, with $d_{GZK} = 130$Mpc for the E_1 case. Examples of scans for the 3° scenario can be seen in Figures 7.9 and 7.10, and the lower limits on the data cuts given deflection scale θ_1 and θ_2 can be seen in Table 7.1. Firstly, we find that we are capable of setting a more constrictive lower bound on the density using the 60EeV data than we are with the 50EeV data. While this result is expected, as higher UHECR energies correspond to shorter travel distances and thus more potential clustering from the reduced number of candidate sources,

E	TS	p-value	$\rho_{bound}\ (\theta_1 = 3°)$	$\rho_{bound}\ (\theta_2 = 30°)$
50EeV	$2.08 \cdot 10^{-2}$	17.30%	$6.19 \cdot 10^{-6}\mathrm{Mpc}^{-3}$	$1.13 \cdot 10^{-6}\mathrm{Mpc}^{-3}$
60EeV	$1.72 \cdot 10^{-2}$	48.95%	$1.44 \cdot 10^{-4}\mathrm{Mpc}^{-3}$	$1.83 \cdot 10^{-5}\mathrm{Mpc}^{-3}$

Table 7.1: Relevant values of the two used data cuts along with lower bounds set on the density of sources using Monte-Carlo data for two deflection scale scenarios.

this is also at least in part due to the lack of an energy spectrum in our simulation. An energy spectrum would effectively further restrict the maximum travel distance for a fraction of the events by allowing them to have energies above 60EeV, which we believe would cause the overall strength of the bound set to been improved to some extent. Additionally, we note that the bounds we set using the E_2 data, compared to Auger's bounds using just $N_{CR} = 83$, are worse by a factor of 3 for θ_1 and better by an order of magnitude for θ_2. This result is similar to what was found in the CR-only case, and most likely pertains to the aforementioned differences in implementation of the magnetic deflection for the two analyses, especially in the θ_2 scenario. It is also important to stress that the E_2 data has $N_{CR} = 149$, with these events covering a larger fraction of the celestial sphere - two factors that further complicate a direct analysis between our lower bounds, and those of Auger. The differences between our result and that of Auger are thus deemed consistent with our differences in implementation.

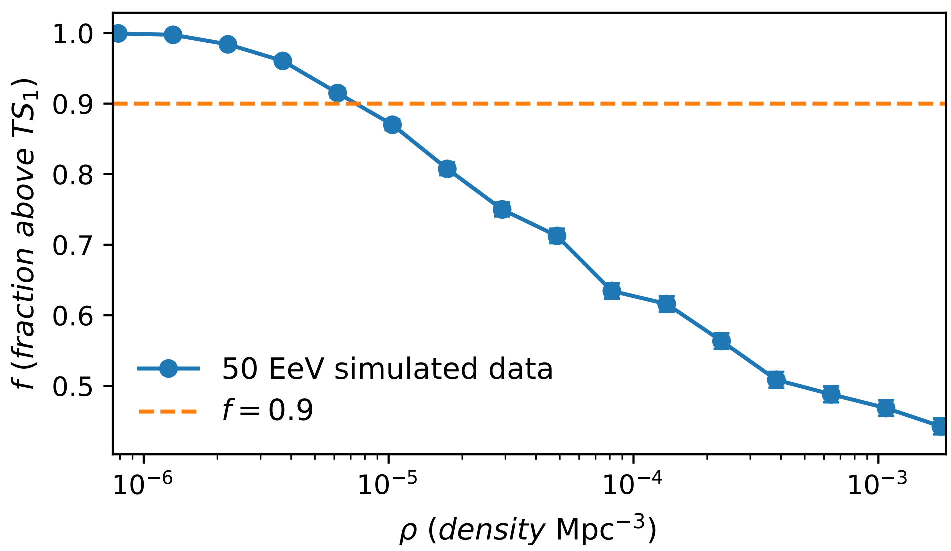

Figure 7.9: Scan over TS_S values from the E_1, θ_1 simulated data to find the point of the lower limit on density.

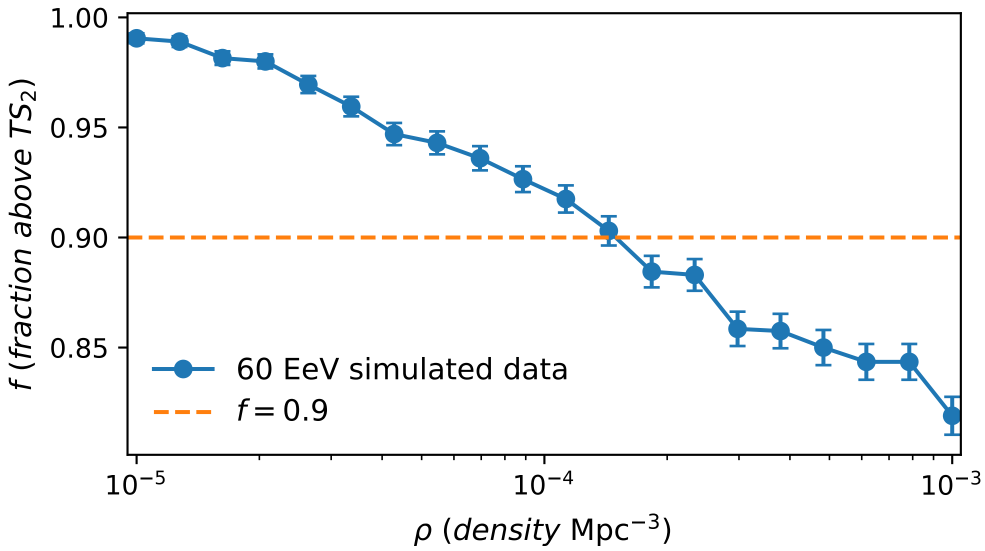

Figure 7.10: Scan over TS_S values from the E_2, θ_1 simulated data to find the point of the lower limit on density.

8 JOINT ANALYSIS

This section will discuss the methods and results specific to the analysis using both the neutrino and CR maps, which we will refer to as the "joint" analysis. The analysis was made using two different test statistics, one based on cross-correlation and the other on maximum likelihood. First these two test statistics will be introduced, and afterwards the results will be presented, followed by a discussion.

8.1 *The cross-correlation TS*

The cross-correlation ('cross-corr') TS is very similar to that of the Kolmogorov-Smirnov TS. The two methods are essentially conceptually identical - they both evaluate the number of pairs on the surface of a sphere within a certain angle of each other. The primary difference, then, is that the autocorrelation correlates a map with itself, while the cross-correlation correlates between two different maps. Otherwise, the mathematics are the same, and Equation 7.4 is used, this time with the cross-spectrum of the two maps instead of the power spectrum. It should be noted that no special care has to be taken to avoid offsets (Equation 7.9) using this method, as the method always pairs different events. An example of a background distribution, along with two signal distributions from actual simulated data can be seen in Figure 8.1.

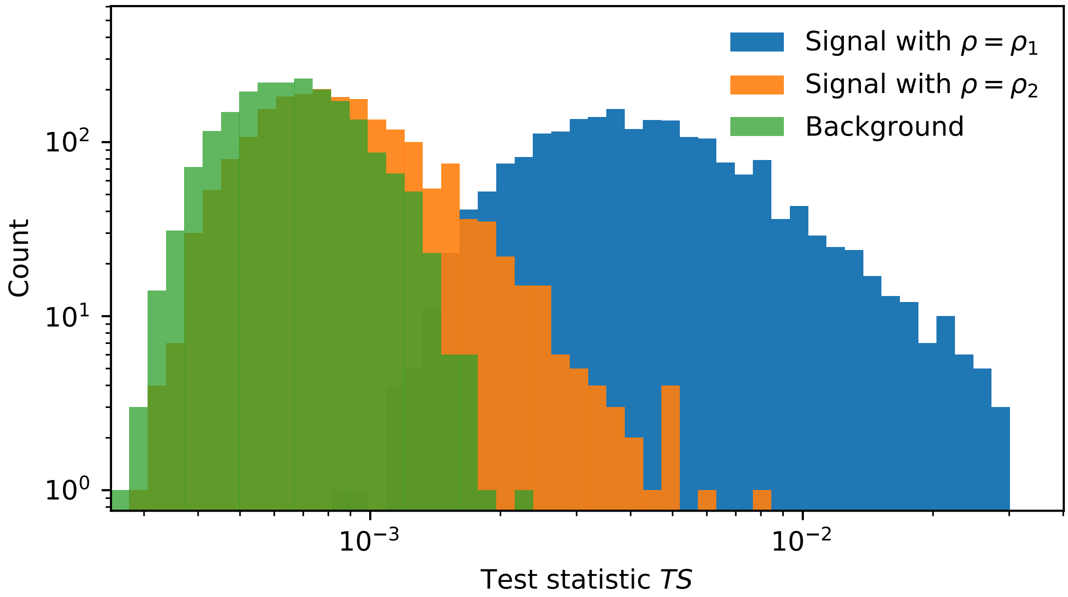

Figure 8.1: Example distributions for background and signal for the cross-correlation KS TS. Taken from simulation with $N_\nu \approx 1400$, $N_{CR} = 150$, $\rho_1 = 10^{-7}\text{Mpc}^{-3}$,$\rho_2 = 5 \cdot 10^{-4}\text{Mpc}^{-3}$ and $n_{samples} = 2000$. The top bin corresponds to the 99th percentile of the signal distribution.

8.2 *The CR template maximum likelihood TS*

The CR template maximum likelihood (MLH) TS is another maximum likehood ratio test, meaning it follows the background expectations that were also true for the all-sky point source TS. The approach goes as follows: the CR map is smoothed by an angle corresponding to the deflection scale used (either 3° or 30°) and normalized. This defines the CR 'template', with local maxima expected in the vicinity of the true direction of a point source. The neutrino map is then correlated with the template map through the likelihood summing over neutrino events

$$\mathcal{L}(n_s) = \sum_{i=1}^{N_\nu} \log\left(xS_i + (1-x)\,B_i\right) \tag{8.1}$$

where S_i is the value of the CR template in the location of the neutrino event and B_i is a simple $\frac{1}{4\pi}$ background expectation. The parameter x denotes the degree to which the neutrino map correlates with the CR template, and is the quantity optimized in the calculation of the test statistic once again given by the ratio $TS = 2\log\left(\frac{\mathcal{L}(1 \geq x \geq 0)}{\mathcal{L}(0)}\right)$. An example of a background distribution, along with two signal distributions from actual simulated data can be seen in Figure 8.2.

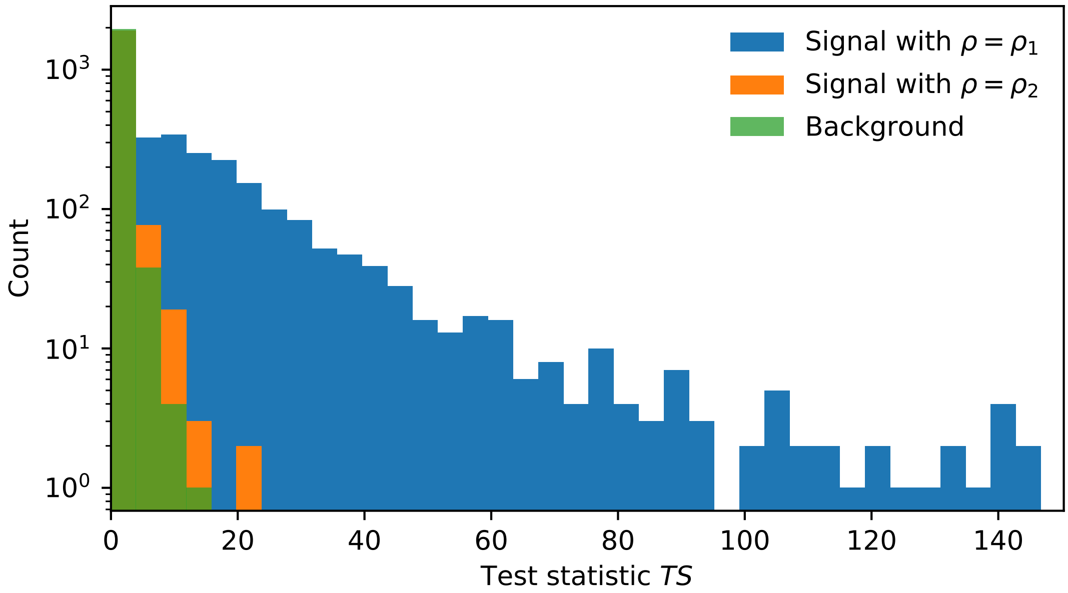

Figure 8.2: Example distributions for background and signal for the CR template MLH TS. Taken from Monte Carlo simulation with $N_\nu \approx 1400$, $N_{CR} = 150$, $\rho_1 = 10^{-7}\text{Mpc}^{-3}$,$\rho_2 = 5 \cdot 10^{-4}\text{Mpc}^{-3}$ and $n_{samples} = 2000$. The top bin corresponds to the 99th percentile of the ρ_1 signal distribution.

8.3 *Results & discussion*

8.3.1 *Basic approach and results*

The joint analysis was carried out using the θ_1 and θ_2 deflection scenarios with the same CR input parameters B, λ, d_{GZK}, $z_{GZK}$and E as were used in the CR-only analysis case. Similar to the ν-only analysis, the signal-to-background ratio S/B was set to 0.1. Since both the number of observed signal cosmic rays N_{CR} and neutrinos N_ν are variable in this analysis, a choice was made to scan over only one of the two, while the other was kept fixed. As the aim is to use high-energy neutrino data to correlate with sparse UHECR data, the number of CRs was kept fixed to $N_{CR} = 150$ for the joint analysis, unless otherwise explicitly stated. In order to be able to compare with the ν-only analysis, the same parameter space was scanned for the joint analysis. Furthermore, in order to ensure that fluctuations from Monte Carlo simulations would not make one method appear superior to another, the simulation was made in such a way that all 4 of the introduced TS-values were evaluated for the same skymaps. Finally, the parameter space was canned over the same range as was the case in the neutrino analysis, using $\rho = 10^{-7} - 10^{-3.3}\text{Mpc}^{-3}$ with $m = 30$ and $N_\nu = 40 - 4 \cdot 10^5$ with $n = 14$. This was done for $n_{samples} = 2000$ Monte Carlo simulations for each combination. The number of samples was selected due to time constraints and available computational resources, and would ideally have been higher. The results in this section will be shown for both joint methods, together with the corresponding sensitivities for the neutrino-only and

Method name	Short form	TS
Joint cross-correlation TS	CR + ν (Cross-correlation)	$TS_{Jnt,1}$
Joint CR template maximum likelihood TS	CR + ν (Max LH CR template)	$TS_{Jnt,2}$
ν-only all-sky max likelihood - PS TS	ν-only (All-sky max LH)	TS_{ν}
CR-only autocorrelation KS TS	CR-only (Autocorrelation)	TS_{CR}

Table 8.1: Table of method names and short hand form used in this section, along with the variable used for their respective test statistics.

CR-only cases for comparison. To avoid any possible confusion, Table 8.1 contains the slighter shorter forms of the names of the methods also used in this section. A final note on the cross-correlation method: it was assumed that evaluation of $TS_{Jnt,1}$ would result in a better sensitivity result when the CR map was correlated with the TS_{ν}-skymap, rather than merely the ν-skymap, and this will be the baseline for all shown $TS_{Jnt,1}$ results unless otherwise stated. This assumption was also tested, and and the results are presented in Section 8.3.3.

Firstly, the sensitivity for the two deflection scenarios θ_1 and θ_2 was computed, and the resulting sensitivity results can be seen in Figures 8.3 and 8.4. The first feature seen in the figures to point out is that the cross-correlation method is entirely independent of the number of signal neutrinos observed until a critical threshold is reached, which seems to roughly coincide with the point of intersection between the sensitivity for the ν-only sensitivity and the cross-correlation sensitivity. It was found that the clustering of CRs drives the cross-correlation sensitivity to a minimum (constant) value, even if the ν-distribution is entirely isotropic. The cross-correlation analysis is thus ineffective until the point where N_{ν} is high enough that nearby point-sources have a significant probability to emit observed multiplets that can correlate with the UHECR events observed in the vicinity of the source. This is largely the same problem that was discussed regarding the ν-only analysis result. Unfortunately, this minimum sensitivity driven by the CR's alone was found to be universally worse than that of the CR autocorrelation. To verify this, data was simulated with a fixed $N_{\nu} = 10^4$ and variable N_{CR} for the θ_1 deflection scenario, see Figure 8.5, which clearly shows the superiority of the autocorrelation method over the cross-correlation method before the N_{ν} threshold is reached.

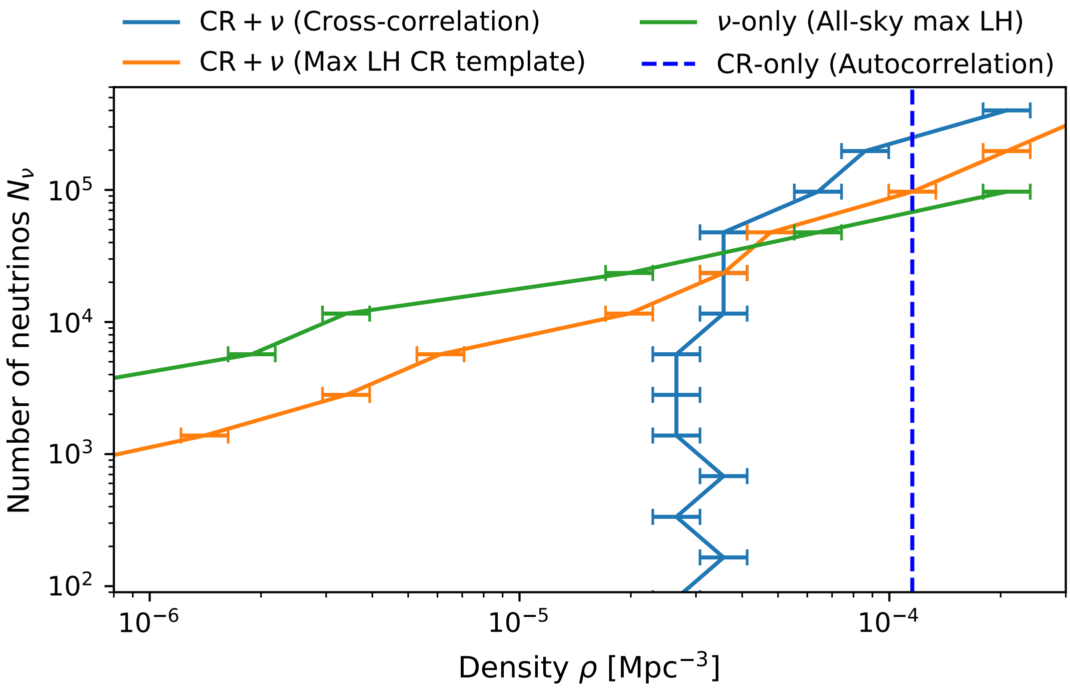

Figure 8.3: Joint sensitivity analysis results for $\theta_s = 3°$, everything to the left of a line is excluded by the analysis. The lines correspond to $TS_{Jnt,1}$, $TS_{Jnt,2}$, TS_ν and TS_{CR} evaluated for the same skymaps generated by Monte Carlo. The straight line for the TS_{CR} result corresponds to the sensitivity at $N_{CR} = 150$.

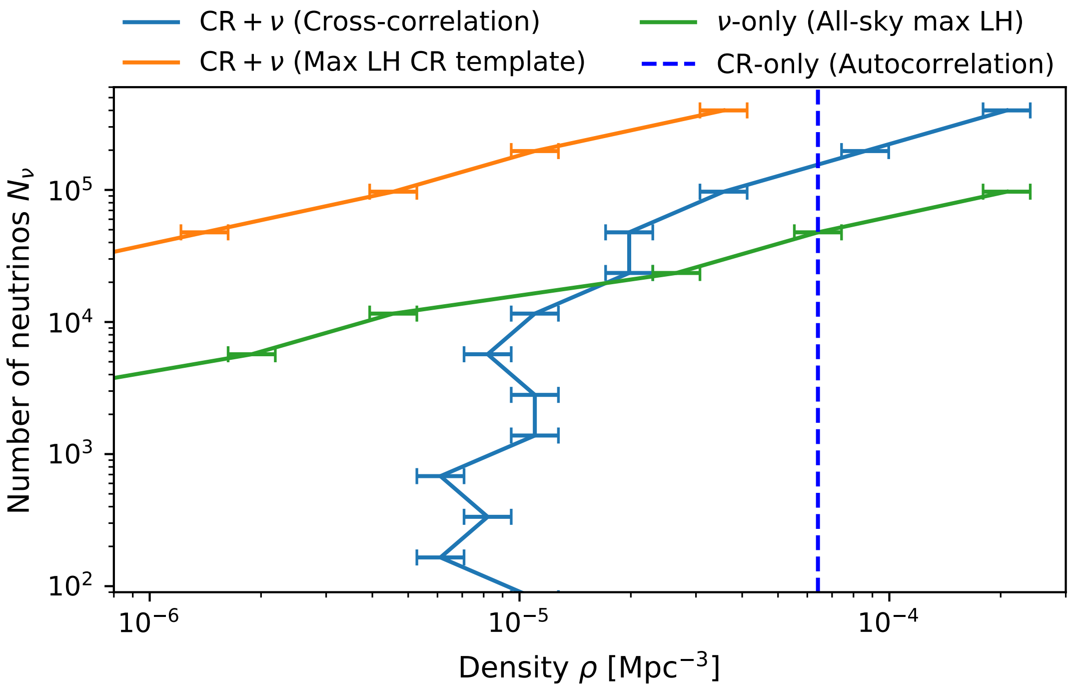

Figure 8.4: Joint sensitivity analysis results for $\theta_s = 30°$, everything to the left of a line is excluded by the analysis. The lines correspond to $TS_{Jnt,1}$, $TS_{Jnt,2}$, TS_ν and TS_{CR} evaluated for the same skymaps generated by Monte Carlo. The straight line for the TS_{CR} result corresponds to the sensitivity at $N_{CR} = 150$.

Another thing to point out is that neither of the joint methods perform better than the combination of the ν- and CR-only analyses. This is especially the case in the θ_2 case, where the CR template MLH method is far from being competitive. In the θ_1 case however, there is only a small disparity between the CR template MLH and the ν-only methods in the density region past the bound set by the CR autocorrelation at $\rho \approx 10^{-4}$, which suggests that it may be possible to tune the joint MLH method to gain increased sensitivity over the ν-only method.

The primary issue with correlating the ν- and CR-maps through either joint method was identified to pertain to the large amount of neutrinos that do not correlate in any way with the CR sources, a result which is in agreement with our initial expectations. Therefore, the effect of attempts at removing the isotropic neutrino background on the sensitivity was investigated. This approach was doubly justified, as it could serve as a means to tune the joint MLH to perform better.

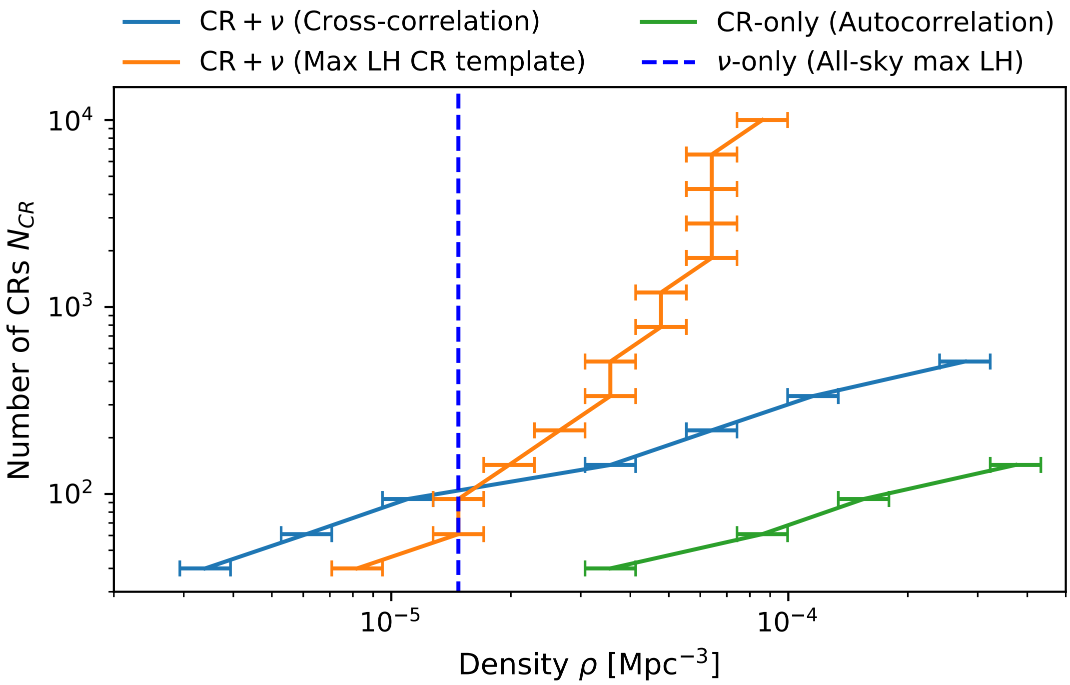

Figure 8.5: Joint sensitivity analysis results for $\theta_s = 3°$, everything to the left of a line is excluded by the analysis. Run with fixed $N_\nu = 10^4$, with the corresponding TS_ν sensitivity given by the dashed vertical line.

8.3.2 *Neutrino–map cleaning*

This was achieved by implementing a basic algorithm that 'cleaned' the neutrino data, i.e. removed neutrinos identified as likely to be uncorrelated with any UHE-CRs. Ít did so by taking the nth percentiles of the ν- and TS_ν-maps' pixel values, and then set all pixels below these values to 0. Effectively, at low N_ν, this method has no impact, as the probability for multiplets is very low, meaning that the value is going to be either 0 or 1 unless very high percentiles are used, effectively setting only value-0 pixels to 0. At higher N_ν however, this has the effect of removing what can be assumed to be an isotropic background, hopefully leaving primarily 'true' neutrino point sources in the neutrino- and TS_ν-maps for correlation with UHE-CRs. It was found that the sensitivity of both of the joint methods was improved by the cleaning method, and the results for 99.5 percentile cleaning used on the joint MLH method can be seen in Figure 8.6. In the figure, there is a clearly noticable disconnect between the uncleaned and cleaned MLH method, and it seems that the MLH method with cleaning is superior to the ν-only method in the range $\rho \approx 10^{-4} - 2 \cdot 10^{-4}$Mpc. In order to verify the gain in sensitivity in the region past $\rho = 10^{-4}$Mpc^{-3}, a high-resolution scan was made in the $\rho = 10^{-4} - 4 \cdot 10^{-4}$Mpc^{-3} and $N_\nu = 4 \cdot 10^4 - 3 \cdot 10^5$ ranges. The resulting sensitivity can be seen in Figure 8.7. Note that it was found that the sensitivity for the MLH method extended outside the scanned area, but due to time constraints, it was not possible to scan a new N_ν region. Regardless of this, the figure clearly shows that there is a region wherein the cleaned joint MLH method is superior to the combined sensitivity of the ν- and CR-only methods. The figure also clearly shows that the joint cross-correlation method remains uncompetitive, even with the cleaning method applied to it. In either case, this result showcases that there is added sensitivity to be gained from cleaning the neutrino map for a joint correlation analysis, and it is worth stressing that a more sophisticated cleaning method might well improve the sensitivity further than what has been showcased here. This is an important result, as the joint cross-correlation analysis run by IceCube, Auger and TA does not utilize any neutrino cleaning [10, 52], which our investigation has shown may improve the strength of current or future analyses.

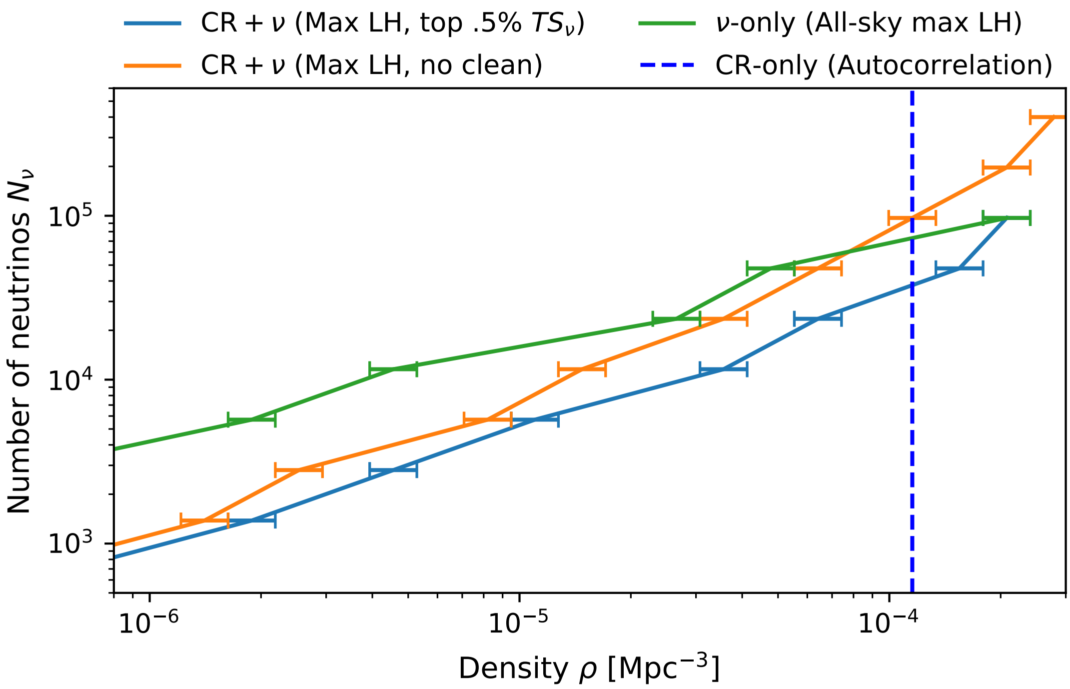

Figure 8.6: CR template MLH results for $\theta_s = 3°$, without cleaning and with 99.5th percentile cleaning.

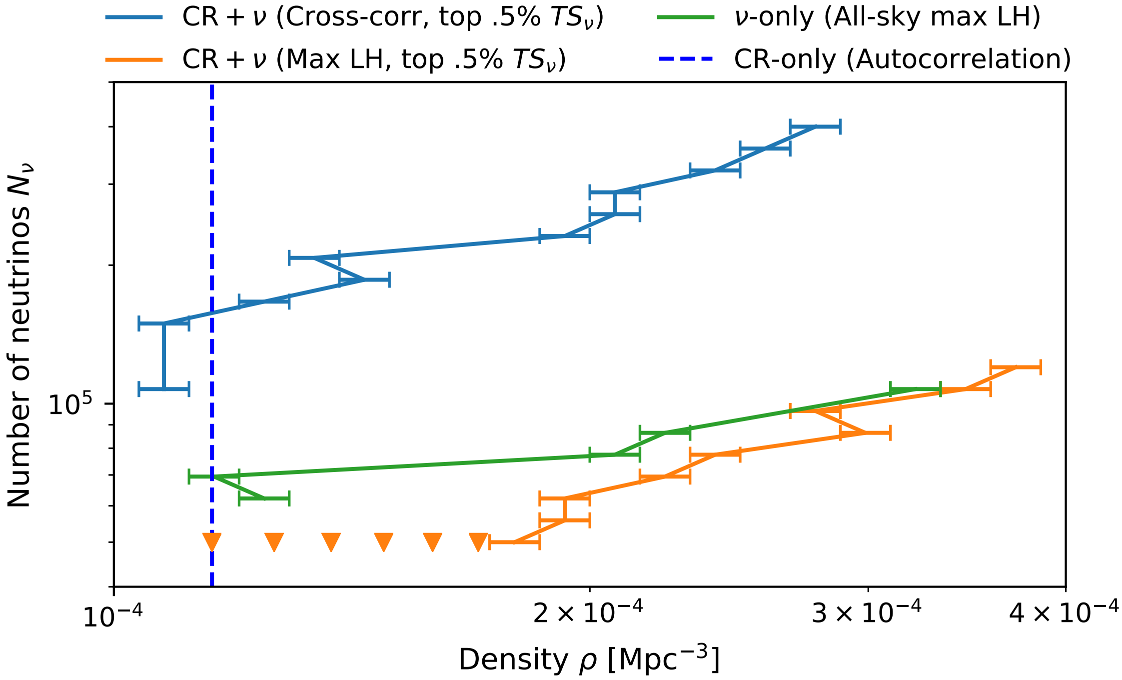

Figure 8.7: Joint sensitivity results at high resolution around $\rho = 10^{-4}\mathrm{Mpc}^{-3}$ with 99.5th percentile cleaning. The MLH result stops around $\rho = 2 \cdot 10^{-4}\mathrm{Mpc}^{-3}$ because it went outside the scanned area. For visual aid, the triangles indicate that the sensitivity line is below the corresponding N_ν value.

To further investigate the potential power of this method for future telescopes with better background data filtering methods, the analysis was repeated with the same cleaning setup, but without any purely background neutrinos in the ν-map (i.e. $S/B = \infty$). The resulting sensitivity for such an ideal case using both joint methods can be seen in Figure 8.8. It can be seen that both joint methods' sensitivity improves by about half an order of magnitude, making them competitive with the CR autocorrelation method around $N_\nu \approx 10^4$. The joint MLH method is still significantly better than the cross-correlation method however. Another interesting thing to note here is that the joint MLH method still seems to outperform the ν-only all-sky MLH around the region of interest at $\rho \approx 10^{-4}\,\mathrm{Mpc}^{-3}$, suggesting that the strength of the cleaning method persists even in low-background cases.

Finally on the topic of cleaning methods, it should be mentioned that a more sophisticated cleaning method using the corresponding χ^2-probability of individual TS_ν-values in each pixel to scale their impact on the joint sensitivity methods was attempted, but this method was comparatively worse than a simple percentile-based cleaning. Using an 'extreme' clean with the 100th percentile, effectively cutting away all pixels below the maximum pixel value, was also implemented, though this method proved to be ineffective as well. Finally, more conservative cleaning attempts, using the 95th and 98th percentile, were also made, though these proved less effective than the 99.5th percentile clean.

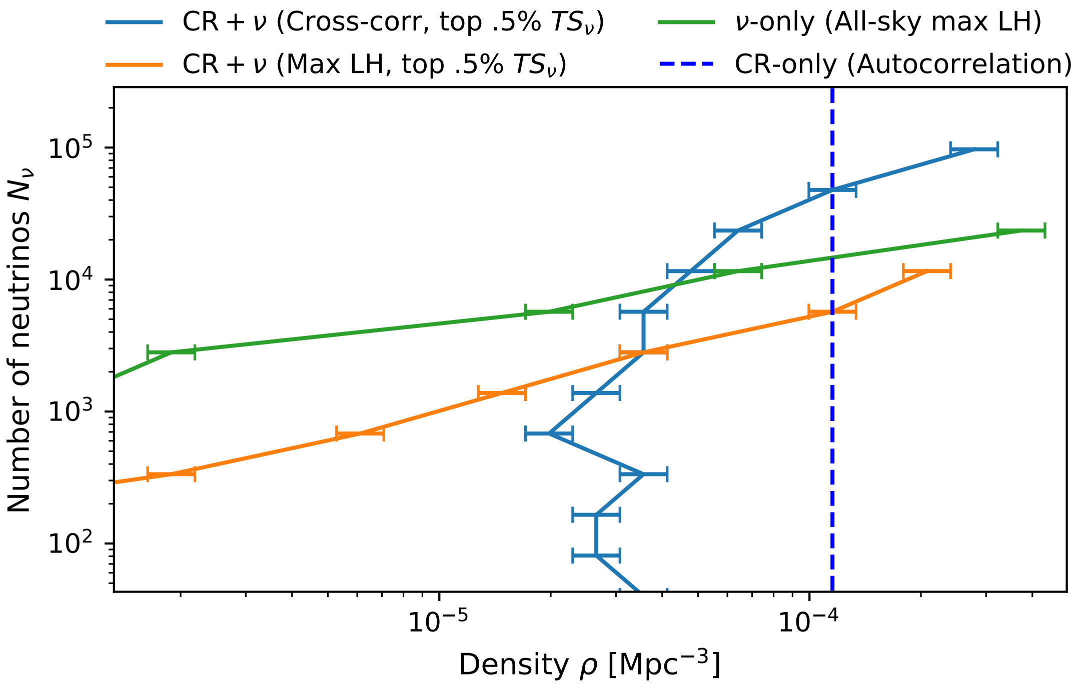

Figure 8.8: Joint analysis results for $\theta_s = 3°$, with 99.5th percentile cleaning and $S/B = \infty$.

8.3.3 *Cross-correlation comparison*

In addition to testing the impact of the cleaning method, the impact of cross-correlating with the TS_ν-skymap over the ν-skymap was also briefly investigated. The improvement from cross-correlating with the TS_ν-map over correlating with the ν-map can be seen in Figure 8.9. The figure shows a significant improvement in using the TS_ν map for cross-correlation over using the ν-map itself, confirming initial suspicions. Furthermore, the plot also shows some improvement from using a cleaning method for the cross-correlation method. This result is yet another example of a potential improvement that can be made to the IceCube, Auger and TA cross-correlation analysis [10, 52]. Their analysis correlates using the ν-map as opposed to the TS_ν-map, which our results suggests is a significantly more powerful method of correlation.

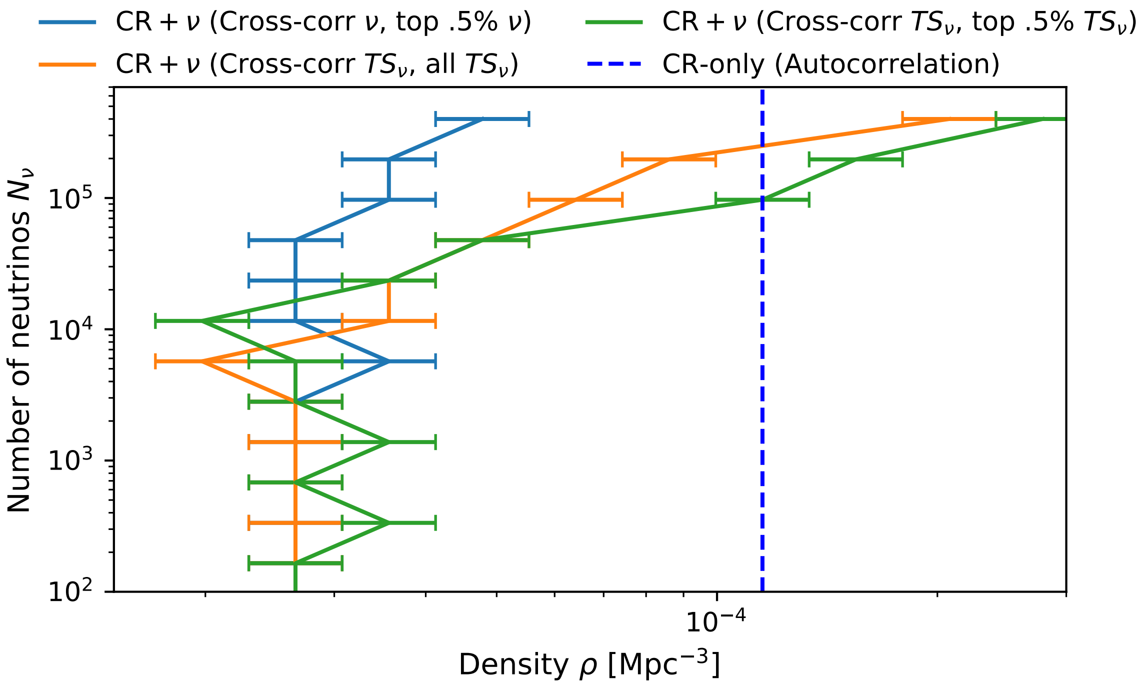

Figure 8.9: Cross correlation results using both the ν-map or the TS_ν-map with both no cleaning applied, and a 99.5th percentile clean.

9 SUMMARY AND OUTLOOK

In this thesis we have investigated the sensitivities of various methods for searching for point sources and anisotropies of UHECR sources by using neutrinos, UHECRs, and both species simultanouesly in a joint analysis. This was done using a realistic, albeit simplified Monte Carlo implementation which allowed for statistical analysis, given the primary variables of number of signal particles observed, N_ν and N_{CR}, and the density of sources, ρ. Secondary variables pertain to the magnetic deflection of UHECRs, the impact of the GZK effect and the signal-to-background ratio of neutrinos.

In accordance with our expectations, we found that analyses involving neutrinos require a large N_ν, in the order of 10^4 signal neutrinos and above, before the 90% sensitivity level is reached for source densities not excluded by previous analyses [49]. In addition, we have shown that the sensitivity of such analyses can improve by around one order of magnitude with the removal of background neutrinos. While observing such high N_ν is unrealistic with contemporary neutrino observatories, it is expected that the next generation of neutrino observatories, such as IceCube Gen2 and KM3NeT [14, 15], could make the observation of point sources possible. In addition, these new observatories will also operate with improved technology and analysis techniques, decreasing the degree to which background neutrinos pollute observational data, which will further improve the prospects of neutrino astronomy.

For analyses using CRs, two deflection scenarios with characteristic deflections, $\theta_1 = 3^\circ$ and $\theta_2 = 30^\circ$ were investigated. Both scenarios assumed protons as the primary constituents of the observed UHECR flux, and differed through whether the rGMF or EGMF was the dominant source of magnetic deflections for UHECRs, respectively. In our CR-only analyses, we found sensitivies and density bounds that were dissimilar to the density bounds set by Auger [49], though these differences could be explained by our differences in sample size and implementation of magnetic deflections. The lower bounds on density were found to be $\rho = 1.44 \cdot 10^{-4}\text{Mpc}^{-3}$ for θ_1 and $\rho = 1.83 \cdot 10^{-5}\text{Mpc}^{-3}$ for θ_2.

The primary results of the thesis pertain to the investigation of the ability to correlate neutrinos and UHECRs. Two different correlation methods were used on neutrinos and UHECRs in simulation, primarily focusing on the θ_1 deflection scenario, and it was found that in general, our MLH CR template method provided better sensitivity than our cross-correlation method. While the baseline joint methods were found to be less effective than the combined sensitivity of the ν- and CR-only methods, we were able to show that the MLH CR template method could provide added sensitivity in our simulation over the combined ν- and CR-only results. This was achieved with the implementation of a simple 'cleaning' method that removed neutrinos assumed to be isotropic and uncorrelated with UHECRs. In addition, we were also able to show that cross-correlating CRs with the TS_ν-map provided better sensitivity than cross-correlating with the ν-map for our simulation. Neither the cleaning algorithm, nor cross-correlating with the TS_ν are methods utilized in the current cross-correlation analysis between neutrinos and UHECRs [10, 52], and it is possible that future analyses could be improved by the implementation of either of these methods.

Finally, it is worth noting that numerous avenues of investigation pertaining to the work done in this thesis still remain unstudied. These include an investigation of deflections scenarios based on a heavier composition hypothesis. In effect, this would mean scaling all deflections by the charge Z, which for $Z = 10$ would set a minimum deflection to 25.9° due to the rGMF. Such an analysis would provide results more comparable to the $\theta = 30°$ results of Auger. Furthermore, the cleaning method implementation was not investigated exhaustively, and it is likely that it could be improved upon further through in-depth study. In addition, the Monte Carlo implementation could be made more sophisticated, e.g. with the implementation of sources following large-scale structure, UHECRs following an energy spectrum, and a more realistic implementation of the GZK effect, focused for instance on the interplay between the GZK effect and increased travel paths caused by magnetic deflection. Lastly, the statistics of several results could be improved upon simply by increasing the number of Monte Carlo samples.

10 BIBLIOGRAPHY

REFERENCES

[1] V. F. Hess, "Uber Beobachtungen der durchdringenden Strahlung bei sieben Freiballonfahrten," *Phys. Z.* **13** (1912) 1084–1091.

[2] J. Linsley, "Evidence for a primary cosmic-ray particle with energy 10**20-eV," *Phys. Rev. Lett.* **10** (1963) 146–148.

[3] K. Greisen, "End to the cosmic ray spectrum?," *Phys. Rev. Lett.* **16** (1966) 748–750.

[4] G. T. Zatsepin and V. A. Kuzmin, "Upper limit of the spectrum of cosmic rays," *JETP Lett.* **4** (1966) 78–80. [Pisma Zh. Eksp. Teor. Fiz.4,114(1966)].

[5] **Pierre Auger** Collaboration, A. Aab *et. al.*, "Searches for Anisotropies in the Arrival Directions of the Highest Energy Cosmic Rays Detected by the Pierre Auger Observatory," *Astrophys. J.* **804** (2015), no. 1 15, 1411.6111.

[6] R. Jansson and G. R. Farrar, "A New Model of the Galactic Magnetic Field," *Astrophys. J.* **757** (2012) 14, 1204.3662.

[7] A. Neronov and I. Vovk, "Evidence for strong extragalactic magnetic fields from Fermi observations of TeV blazars," *Science* **328** (2010) 73–75, 1006.3504.

[8] J. Blumer, R. Engel, and J. R. Horandel, "Cosmic Rays from the Knee to the Highest Energies," *Prog. Part. Nucl. Phys.* **63** (2009) 293–338, 0904.0725.

[9] L. A. Anchordoqui and T. Montaruli, "In Search for Extraterrestrial High Energy Neutrinos," *Ann. Rev. Nucl. Part. Sci.* **60** (2010) 129–162, 0912.1035.

[10] **IceCube, Pierre Auger, Telescope Array** Collaboration, M. G. Aartsen *et. al.*, "Search for correlations between the arrival directions of IceCube neutrino events and ultrahigh-energy cosmic rays detected by the Pierre Auger Observatory and the Telescope Array," *JCAP* **1601** (2016), no. 01 037, 1511.09408.

[11] **IceCube** Collaboration, A. Achterberg *et. al.*, "First Year Performance of The IceCube Neutrino Telescope," *Astropart. Phys.* **26** (2006) 155–173, astro-ph/0604450.

[12] **IceCube** Collaboration, M. G. Aartsen *et. al.*, "Evidence for High-Energy Extraterrestrial Neutrinos at the IceCube Detector," *Science* **342** (2013) 1242856, 1311.5238.

[13] **IceCube, Fermi-LAT, MAGIC, AGILE, ASAS-SN, HAWC, H.E.S.S., INTEGRAL, Kanata, Kiso, Kapteyn, Liverpool Telescope, Subaru, Swift NuSTAR, VERITAS, VLA/17B-403** Collaboration, M. G. Aartsen *et. al.*, "Multimessenger observations of a flaring blazar coincident with high-energy neutrino IceCube-170922A," *Science* **361** (2018), no. 6398 eaat1378, 1807.08816.

[14] **IceCube** Collaboration, M. G. Aartsen *et. al.*, "IceCube-Gen2: A Vision for the Future of Neutrino Astronomy in Antarctica," `1412.5106`.

[15] **KM3Net** Collaboration, S. Adrian-Martinez *et. al.*, "Letter of intent for KM3NeT 2.0," *J. Phys.* **G43** (2016), no. 8 084001, `1601.07459`.

[16] R. M. Bionta *et. al.*, "Observation of a Neutrino Burst in Coincidence with Supernova SN 1987a in the Large Magellanic Cloud," *Phys. Rev. Lett.* **58** (1987) 1494.

[17] E. N. Alekseev, L. N. Alekseeva, I. V. Krivosheina, and V. I. Volchenko, "Detection of the Neutrino Signal From SN1987A in the LMC Using the Inr Baksan Underground Scintillation Telescope," *Phys. Lett.* **B205** (1988) 209–214.

[18] **Super-Kamiokande** Collaboration, Y. Fukuda *et. al.*, "Evidence for oscillation of atmospheric neutrinos," *Phys. Rev. Lett.* **81** (1998) 1562–1567, `hep-ex/9807003`.

[19] **Super-Kamiokande** Collaboration, Y. Fukuda *et. al.*, "The Super-Kamiokande detector," *Nucl. Instrum. Meth.* **A501** (2003) 418–462.

[20] **ANTARES** Collaboration, M. Ageron *et. al.*, "ANTARES: the first undersea neutrino telescope," *Nucl. Instrum. Meth.* **A656** (2011) 11–38, `1104.1607`.

[21] **LIGO Scientific** Collaboration, B. P. Abbott *et. al.*, "LIGO: The Laser interferometer gravitational-wave observatory," *Rept. Prog. Phys.* **72** (2009) 076901, `0711.3041`.

[22] **Pierre Auger** Collaboration, A. Aab *et. al.*, "The Pierre Auger Cosmic Ray Observatory," *Nucl. Instrum. Meth.* **A798** (2015) 172–213, `1502.01323`.

[23] **Telescope Array** Collaboration, H. Kawai *et. al.*, "Telescope array experiment," *Nucl. Phys. Proc. Suppl.* **175-176** (2008) 221–226.

[24] L. A. Anchordoqui, "Ultra-High-Energy Cosmic Rays," `1807.09645`.

[25] **Fermi-LAT** Collaboration, M. Ackermann *et. al.*, "Detection of the Characteristic Pion-Decay Signature in Supernova Remnants," *Science* **339** (2013) 807, `1302.3307`.

[26] **AMS** Collaboration, M. Aguilar *et. al.*, "The Alpha Magnetic Spectrometer (AMS) on the International Space Station. I: Results from the test flight on the space shuttle," *Phys. Rept.* **366** (2002) 331–405. [Erratum: Phys. Rept.380,97(2003)].

[27] T. K. Gaisser, R. Engel, and E. Resconi, *Cosmic Rays and Particle Physics*. Cambridge University Press, second ed., 2016.

[28] **LIGO Scientific, Virgo** Collaboration, B. P. Abbott *et. al.*, "GW150914: First results from the search for binary black hole coalescence with Advanced LIGO," *Phys. Rev.* **D93** (2016), no. 12 122003, `1602.03839`.

[29] R.-G. Cai, Z. Cao, Z.-K. Guo, S.-J. Wang, and T. Yang, "The Gravitational-Wave Physics," *Natl. Sci. Rev.* **4** (2017), no. 5 687–706, `1703.00187`.

[30] **Particle Data Group** Collaboration, M. Tanabashi *et. al.*, "Review of Particle Physics," *Phys. Rev.* **D98** (2018), no. 3 030001.

[31] J. K. Becker, "High-energy neutrinos in the context of multimessenger physics," *Phys. Rept.* **458** (2008) 173–246, `0710.1557`.

[32] A. M. Hillas, "The Origin of Ultrahigh-Energy Cosmic Rays," *Ann. Rev. Astron. Astrophys.* **22** (1984) 425–444.

[33] **IceCube** Collaboration, M. G. Aartsen *et. al.*, "Probing the origin of cosmic rays with extremely high energy neutrinos using the IceCube Observatory," *Phys. Rev.* **D88** (2013) 112008, `1310.5477`.

[34] E. Fermi, "On the Origin of the Cosmic Radiation," *Phys. Rev.* **75** (1949) 1169–1174.

[35] A. R. Bell, "The Acceleration of cosmic rays in shock fronts. I," *Mon. Not. Roy. Astron. Soc.* **182** (1978) 147–156.

[36] M. S. Longair, *High-energy astrophysics*. Cambridge University Press, third ed., 2011.

[37] A. De Angelis, G. Galanti, and M. Roncadelli, "Transparency of the Universe to gamma rays," *Mon. Not. Roy. Astron. Soc.* **432** (2013) 3245–3249, `1302.6460`.

[38] M. Ahlers and F. Halzen, "High-energy cosmic neutrino puzzle: a review," *Rept. Prog. Phys.* **78** (2015), no. 12 126901.

[39] **Planck** Collaboration, P. A. R. Ade *et. al.*, "Planck 2015 results. XIII. Cosmological parameters," *Astron. Astrophys.* **594** (2016) A13, `1502.01589`.

[40] D. W. Hogg, "Distance measures in cosmology," `astro-ph/9905116`.

[41] H. Yuksel, M. D. Kistler, J. F. Beacom, and A. M. Hopkins, "Revealing the High-Redshift Star Formation Rate with Gamma-Ray Bursts," *Astrophys. J.* **683** (2008) L5–L8, `0804.4008`.

[42] Y. Hoffman, E. Carlesi, D. Pomarede, R. B. Tully, H. M. Courtois, S. Gottlober, N. I. Libeskind, J. G. Sorce, and G. Yepes, "The quasi-linear nearby Universe," *Nat. Astron.* **2** (2018), no. 8 680–687, `1807.03724`.

[43] M. Ahlers and F. Halzen, "Pinpointing Extragalactic Neutrino Sources in Light of Recent IceCube Observations," *Phys. Rev.* **D90** (2014), no. 4 043005, `1406.2160`.

[44] E. Waxman and J. Miralda-Escude, "Images of bursting sources of high-energy cosmic rays. 1. Effects of magnetic fields," *Astrophys. J.* **472** (1996) L89–L92, `astro-ph/9607059`.

[45] M. C. Beck, A. M. Beck, R. Beck, K. Dolag, A. W. Strong, and P. Nielaba, "New constraints on modelling the random magnetic field of the MW," *JCAP* **1605** (2016), no. 05 056, 1409.5120.

[46] M. S. Pshirkov, P. G. Tinyakov, and F. R. Urban, "Mapping UHECRs deflections through the turbulent galactic magnetic field with the latest RM data," *Mon. Not. Roy. Astron. Soc.* **436** (2013) 2326, 1304.3217.

[47] R. Durrer and A. Neronov, "Cosmological Magnetic Fields: Their Generation, Evolution and Observation," *Astron. Astrophys. Rev.* **21** (2013) 62, 1303.7121.

[48] M. Ahlers, Y. Bai, V. Barger, and R. Lu, "Galactic neutrinos in the TeV to PeV range," *Phys. Rev.* **D93** (2016), no. 1 013009, 1505.03156.

[49] **Pierre Auger** Collaboration, P. Abreu *et. al.*, "Bounds on the density of sources of ultra-high energy cosmic rays from the Pierre Auger Observatory," *JCAP* **1305** (2013), no. 05 009, 1305.1576.

[50] J. Braun, J. Dumm, F. De Palma, C. Finley, A. Karle, and T. Montaruli, "Methods for point source analysis in high energy neutrino telescopes," *Astropart. Phys.* **29** (2008) 299–305, 0801.1604.

[51] S. S. Wilks, "The Large-Sample Distribution of the Likelihood Ratio for Testing Composite Hypotheses," *Annals Math. Statist.* **9** (1938), no. 1 60–62.

[52] D. Veberic, ed., *The IceCube Neutrino Observatory, the Pierre Auger Observatory and the Telescope Array: Joint Contribution to the 35th International Cosmic Ray Conference (ICRC 2017)*, 2018.

[53] **IceCube** Collaboration, M. G. Aartsen *et. al.*, "All-sky Search for Time-integrated Neutrino Emission from Astrophysical Sources with 7 yr of IceCube Data," *Astrophys. J.* **835** (2017), no. 2 151, 1609.04981.

[54] **IceCube** Collaboration, M. G. Aartsen *et. al.*, "Search for steady point-like sources in the astrophysical muon neutrino flux with 8 years of IceCube data," *Eur. Phys. J.* **C79** (2019), no. 3 234, 1811.07979.

[55] P. Sommers, "Cosmic ray anisotropy analysis with a full-sky observatory," *Astropart. Phys.* **14** (2001) 271–286, astro-ph/0004016.

A APPENDIX

A.1 *Link to 'ordinary' flux equation*

Having

$$\lambda_{PS,E} = \frac{1}{4\pi d_L^2} \int_0^\infty E\,(1+z)^2\, Q\left((1+z)\,E\right)\ \mathrm{d}E$$

One can move to the reference frame of the emitting source by substituting $E' = (1+z)\,E$ and $\mathrm{d}E' = (1+z)\,\mathrm{d}E$, yielding:

$$\lambda_{PS,E} = \frac{1}{4\pi d_L^2} \int_0^\infty E' Q\left(E'\right)\ \mathrm{d}E'$$

where the luminosity of the source is given by $L = \int_0^\infty E' Q\left(E'\right)\ \mathrm{d}E'$.

A.2 *Rotation matrix derivation*

Consider a unit sphere. We have colatitude and longitude, meaning that the north pole $(0,0,1)$ in Cartesian coordinate is given by $(\phi,\theta) = (0,0)$ in spherical coordinates. We then imagine a point at the north pole of the sphere, we call this point p. An angular distance α away from point p, we define a circle on the surface of the sphere. This circle will be parametrized by spherical coordinates $(\phi,\theta) = (t,\alpha)$, where $0 \le t \le 2\pi$. Converting to Cartesian coordinates yields:

$$\begin{pmatrix} x \\ y \\ z \end{pmatrix} = \begin{pmatrix} \sin\alpha\cos t \\ \sin\alpha\sin t \\ \cos\alpha \end{pmatrix}$$

We then rotate the polar angle (meaning θ is changed), which is synonymous with rotating about the xz plane, or about the y-axis. The rotation matrix for rotation about the y-axis is given by:

$$R_y\left(\vartheta\right) = \begin{pmatrix} \cos\vartheta & 0 & \sin\vartheta \\ 0 & 1 & 0 \\ -\sin\vartheta & 0 & \cos\vartheta \end{pmatrix}$$

Rotation yields:

$$\begin{pmatrix} \cos\vartheta & 0 & \sin\vartheta \\ 0 & 1 & 0 \\ -\sin\vartheta & 0 & \cos\vartheta \end{pmatrix} \begin{pmatrix} \sin\alpha\cos t \\ \sin\alpha\sin t \\ \cos\alpha \end{pmatrix} = \begin{pmatrix} \cos\vartheta\sin\alpha\cos t + \sin\vartheta\cos\alpha \\ \sin\alpha\sin t \\ -\sin\vartheta\sin\alpha\cos t + \cos\vartheta\cos\alpha \end{pmatrix}$$

Next, we rotate about the azimuthal angle (meaning that ϕ is changed), which is synonymous with rotating about the xy plane, or about the z-axis. The rotation matrix for rotation about the z-axis is given by:

$$R_y\left(\varphi\right) = \begin{pmatrix} \cos\varphi & -\sin\varphi & 0 \\ \sin\varphi & \cos\varphi & 0 \\ 0 & 0 & 1 \end{pmatrix}$$

Rotation yields:

$$
\begin{pmatrix} \cos\varphi & -\sin\varphi & 0 \\ \sin\varphi & \cos\varphi & 0 \\ 0 & 0 & 1 \end{pmatrix} \begin{pmatrix} \cos\vartheta\sin\alpha\cos t + \sin\vartheta\cos\alpha \\ \sin\alpha\sin t \\ -\sin\vartheta\sin\alpha\cos t + \cos\vartheta\cos\alpha \end{pmatrix}
$$

$$
= \begin{pmatrix} \cos\varphi\cos\vartheta\sin\alpha\cos t - \sin\varphi\sin\alpha\sin t + \cos\varphi\sin\vartheta\cos\alpha \\ \sin\varphi\cos\vartheta\sin\alpha\cos t + \cos\varphi\sin\alpha\sin t + \sin\varphi\sin\vartheta\cos\alpha \\ -\sin\vartheta\sin\alpha\cos t + \cos\vartheta\cos\alpha \end{pmatrix}
$$

This is then the position in Cartesian coordinates in the circle at point $(\phi, \theta) = (\varphi, \vartheta)$.